Geochimica et Cosmochimica Acta 387 (2024) 63–82

Contents lists available at ScienceDirect

Geochimica et Cosmochimica Acta

journal homepage: www.elsevier.com/locate/gca

Origin of the Ca-phosphate inclusions in Ivory Coast and Australasian Muong-Nong-type tektites

Pierre-Marie Zanetta [a,b,*], Anne-Magali Seydoux-Guillaume [a], Pierre Rochette [b], Bruno Reynard [a], Victor Tricaud [a], Petanki Soro [b,c], Southone Singsoupho [d], Alain Nicaise Kouamelan [c], Obrou Monda [e], David Baratoux [c,f]

[a] CNRS, Université Jean Monnet Saint-Étienne, ENS de Lyon, LGL-TPE, UMR5276, F-42023 Saint-Etienne, France
[b] Aix-Marseille Université, CNRS, IRD, INRAE, CEREGE, 13545 Aix-en-Provence, France
[c] UFR STRM, Université Félix Houphouët-Boigny, Abidjan-Cocody, 22 B.P. 582, Abidjan 22, Cote d'Ivoire
[d] National University of Laos, Laos
[e] Mineral Analysis Laboratory of SODEMI, 31, Bd des Martyrs, Abidjan-Cocody, 01 BP 2816, Abidjan 01, Cote d'Ivoire
[f] Géosciences Environnement Toulouse, Université de Toulouse, CNRS & IRD, 14, Avenue Edouard Belin, 31 400 Toulouse, France

ARTICLE INFO

Associate editor: Rhian Jones

Keywords:
Tektites
Meteoritic impacts
Mineral inclusions
Glass
Diffusion profiles
Cooling rates

ABSTRACT

Tektites are reduced (Fe^{2+}) glasses formed by the quenching of molten material ejected from Earth's surface as a result of a hypervelocity impact. The vast majority of tektites are usually homogeneous glasses, but rare samples containing mineral inclusions can provide insights about the source material, sample thermal history, and tektite formation process. Tektites from two distinct strewn fields presenting Ca-phosphate inclusions detected from anomalous magnetic susceptibility were studied: one sample from the Ivory Coast tektite (ICT) field ejected at 1.07 Ma from the Bosumtwi crater (10.5 km in size) in Ghana and two Muong Nong type samples from the Australasian tektite field (MN-AAT) ejected at 0.79 Ma from a crater possibly situated in southeast Asia. In ICT, Ca-phosphate inclusions are systematically embedded in lechatelierite (SiO_2 glass). In MN-AAT Ca-phosphate are either embedded in lechatelierite or in Fe-rich glass forming schlieren. Multiscale petrographic characterization using correlative microscopy associating scanning electron microscopy, microprobe and, transmission electron microscopy reveals that rounded inclusions in ivoirite are composed of acicular Ca-phosphates (merrillite) embedded in an amorphous P-rich glass. In MN-AAT, inclusions consist mostly of single droplets of Fe-Mg rich Ca-phosphate (structurally related to apatite), but few droplets often forming an emulsion texture show a complex assemblage of apatite, magnetite, pyroxene, and spinel growing from a Pt-rich nucleus. Diffusion profile around lechatelierite domains reveals maximum temperatures greater than 2200–2400 °C in the impact plume of the Australasian tektite and the Ivory coast tektite. Heating time is of the order of seconds-tens of seconds rather than minutes as previously suggested (20 s for MN-AAT and 5 s for ICT). The number, the density, and the fact that inclusions are entirely crystallized in MN-AAT support relatively slow cooling rates (<200 °C/h), in comparison with the faster cooling rates (>2000 °C/h) indicated by the precipitation of amorphous P-rich glass in ICT. In both impact events, ejecta that had been heated to high temperatures did not remain in the vapor plume for an extended period of time and landed rapidly (within tens of seconds) at a relatively high temperature (>1000 °C) on the Earth's surface.

Phosphate inclusions systematically embedded in lechatelierite in ICT provide clues about the source material. It suggests that the parent material for these silica-rich inclusions is not conventional detrital quartz. Rather, parts of lechatelierite domains may be inherited from a biogenic source that could be consistent with tropical soil (source of the phosphor) and its biomass (silica of plant origin). The reduction process that tektites record during their formation may be explained by superficial material since forests can contain a sizable mass of carbon that can reduce iron in tektites and produce platinoid-rich metallic nuclei and the $Fe^{3+}/\Sigma Fe$ gradient recorded by the dendritic spinels.

* Corresponding author at: Laboratoire de Géologie de Lyon: Terre, Planète, Environnement UMR5276 (CNRS, UCBL1, ENSLyon, UJM Saint-Etienne) Université Jean Monnet (UJM), Faculté des Sciences et Techniques Campus Manufacture - Les Forges II 20 rue Dr Rémy Annino 42023 SAINT-ETIENNE CEDEX 2.
E-mail address: pierre.marie.zanetta@gmail.com (P.-M. Zanetta).

https://doi.org/10.1016/j.gca.2024.09.021
Received 15 January 2024; Accepted 14 September 2024
Available online 18 September 2024

1. Introduction

Tektites are small (cm-sized), impact-generated, homogeneous glass ejecta that commonly contain lechatelierite, i.e. almost pure SiO_2 glass inclusions (Glass, 1990; Kinnunen, 1990; Dressler and Reimold, 2001). They occur in five distinct, geographically confined strewn fields. Four have been the subject of extensive literature in the past, the well-known australasites, ivorites, moldavites, and North American tektites (Howard, 2011). Recently a new tektite strewn field has been identified in Central America; the belizites (Rochette et al., 2021; Koeberl et al., 2022). The Australasian strewn field is the youngest (789 ± 9 ka (Jourdan et al., 2019)) and the largest, covering over 10 % of the surface of the globe if one includes microtektites (Folco et al., 2008). Its source crater is still unknown, and the region where the crater is located remains a matter of contention, although a long-standing consensus place it in Indochina (e.g. Glass and Pizzuto, 1994)). One recent hypothesis locates it in southern Laos, within the Bolaven Plateau (Sieh et al., 2020, 2023). However, strong arguments have been put forth against this hypothesis (Mizera, 2022). Alternative proposed locations are northwest China (Mizera et al., 2016) or Red River offshore basin (Whymark, 2021; Seydoux-Guillaume et al., 2024). The four other strewn fields have been firmly associated with known source craters, ivorites – Bosumtwi (1.07 ± 0.05 Ma), moldavites – Ries (14.808 ± 0.021 Ma), belizites – Pantasma (804 ± 9 ka) and North American tektites – Chesapeake Bay (35.5 ± 0.8 Ma), respectively (Glass, 1990; Koeberl, 1994; Collins and Wünnemann, 2005; Koeberl et al., 2007; Schmieder et al., 2018; Rochette et al., 2021).

Tektites are classified into three groups based on their morphology and texture (Glass, 1990; Koeberl, 1994). The "splash form" tektites (spherical and dumbbell-shaped tektites), the "ablated form" tektites which show on their surface evidence of partial re-melting during atmospheric re-entry and, the "Muong-Nuong type" (MN) tektites, named after well-known tektite-bearing locality in Laos (Fiske et al., 1999). The MN tektites can be considerably larger than the other tektite types and samples up to 24 kg have been reported (Koeberl, 1992, 1994; Fiske et al., 1999). They have a blocky appearance and contain abundant vesicles. Under optical microscope, MN tektites appear layered with lighter and darker layers evidencing chemical heterogeneity in the glass, and some contain mineral inclusions. MN tektites are assumed to have cooled more slowly than other types, which might have facilitated the crystallization of low-miscibility phases in silica-rich glass (Glass, 1990).

The thermal history of tektites is mostly constrained by numerical modeling, chemical diffusion profile between lechatelierite and host glass, calorimetry, and vesicle size distribution (Wilding et al., 1996; Stöffler et al., 2002; Macris et al., 2018; Masotta et al., 2020). The presence of contorted lechatelierite in the host glass indicates that the source material has been rapidly heated (< few seconds) to a high temperature (>1800 °C) and then quickly (<few minutes or hours) cooled (Glass, 1990; Wilding et al., 1996; Macris et al., 2018). One challenge in deciphering the tektite formation process is that the thermal history can fluctuate not only between samples but also within a single sample. Thus, the specificities of the tektite generation process, especially at the time of the impact, are not well understood. A puzzling question about the process forming tektites relates to their oxidation state. Iron in tektites is mostly present as Fe^{2+}, or even metal with ferromagnetic impurities in the order of 10 ppm at most, while Fe^{3+} if present is very minor (Chao et al., 1962; Rochette et al., 2015, 2019). However, evidence from cosmogenic ^{10}Be indicates that tektite is produced by melting the first meters of the continental surface (mixed with limited extent of deeper material), made of weathered rocks where iron is mostly in Fe^{3+} form (Rochette et al., 2018). Thus, the process that produces tektites involves a reduction reaction, and two main mechanisms have been proposed so far. The first mechanism is the breakdown of the Fe_2O_3 throughout isentropic cooling of vapor and liquid during the decompression stage following shock compression (Engelhardt et al., 1987; Lukanin and Kadik, 2007; Sheffer, 2007). The second proposed process involves the combustion of biomass during tektite formation, but this has never been firmly established (Kinnunen, 1990; Žák et al., 2012; Rochette et al., 2015; Mizera and Řanda, 2022).

Investigating samples across strewn fields provides access to variable dynamical and thermal histories in the tektite generation process, particularly when characteristic mineralogical, compositional, and textural tracers can be identified. This study focuses on inclusion-bearing tektites from the ivorite and Australasite tektite fields. **The Ivory Coast tektites (ICTs)**, ejected from the Bosumtwi crater (10.5 km in size) in Ghana, present various shapes (teardrops, dumbbells, spheres, ellipsoids). ICTs have long been thought to be chemically homogeneous with a relatively low SiO_2 content (~68 wt%) (Barnes, 1961, 1963; Koeberl, 1990, 1992). A recent field study, however, led to the discovery of several tens of tektites, extended the known limits of the strewn field, and revealed a more variable chemical composition than the apparent homogeneity previously inferred from a more limited number of samples (Soro et al., 2023). The maximum ejection distance of tektites is estimated to be 340 km away from the Bosumtwi crater. **The Australasian tektites** vary largely in composition and are chemically and isotopically distinct from other tektite strewn fields (Koeberl, 1990, 1992; Soro et al., 2023). They are high-Si glass, with average SiO_2 73.5 wt%. The source crater of the Australasian strewn field is estimated to be larger [10–115 km] than the Bosumtwi crater [10.5 km], with recent estimation >30km e.g., (Mizera et al., 2016), since these tektites have been ejected to more than 5000 km around the possible impact locations (Glass, 1990; Glass and Pizzuto, 1994; Koeberl, 1994; Mizera et al., 2016). The presence of mineral inclusions in tektites is of interest because it can provide new insights into the sample's thermal history and can be a potential indicator of the source material (Glass and Barlow, 1979). Exceptional samples containing mineral inclusions are therefore windows into crucial stages of impact and tektite formation.

Here, we investigated mineral inclusions found in anomalous tektites identified through magnetic susceptibility screening among large tektite collections. We used correlative microscopy [scanning electron microscope (SEM), electron microprobe (EPMA), focused ion beam scanning electron microscope (FIB-SEM), and aberration-corrected scanning-transmission electron microscope (TEM/STEM)] to provide a multiscale petrographic description of the studied tektites. We report the presence of Ca-phosphate inclusions in a splash-type spherical ivorite and a Muong Nong-type Australasian tektite (MN-AAT). To our knowledge, this is the first time that mineral inclusions of this sort have been described in tektites. The microstructure of these inclusions provides information on cooling rates and thermal history of the two tektites. We discuss the potential origin of these phosphates.

2. Sample and methods

Magnetic susceptibility (χ) measurements were obtained on a large tektite collection (see Rochette et al., (2015, 2019) and Soro et al., (2023) for the methodology) to document possible outliers in terms of total iron content or ferromagnetic inclusions. Hysteresis measurements were performed on the high-susceptibility samples using a Micromag VSM in CEREGE laboratory (France). A 3 g Ivory Coast tektite (splash-form type) from the Société des Mines de Côte d'Ivoire (SODEMI) collection in Abidjan (Soro et al., 2023) and two Muong Nong type AAT samples (MN-AAT1 and MN-AAT2), from the N19 site near Muong Nong (Laos), were identified as anomalous. N19 is a lateritic gravel quarry where we collected in 2019 numerous fragments totaling 152 g (the largest is 36 g), very close to the N20 site mentioned by Masotta et al., (2020). Hereafter, we will refer to the ivorite sample as ICT. The two samples (MN-AAT1 and MN-AAT2) show similar characteristics in composition and in phase assemblages found within the inclusions at the SEM and TEM scale. They have been grouped under the MN-AAT denomination. Both ICT and MM-AAT were sorted out from a database of several hundreds of samples. Polished slices of these 3 (sub) samples embedded in epoxy resin were prepared for optical and electron

microscopy. Bulk analyses of major and trace elements were obtained on the powdered sub-samples using inductively-coupled plasma-mass spectrometer (ICP-MS) and Auger electron spectroscopy in Geotime Brussels (for MN-AAT) and SARM Nancy (for ICT). Approximately 50 mg of crushed material was dissolved by alkaline fusion using ultrapure (>99.99%) lithium metaborate. Major elements were measured using a Thermo Scientific ICaP (inductively-coupled plasma atomic emission spectroscopy). Loss on ignition was measured after 1 h at 1000 °C and corrected for Fe content. For trace elements, the concentrations were measured on an Agilent 7700 quadrupole inductively-coupled plasma-mass spectrometer (ICP-MS). International standards BCR-2, AGV-2 and BHVO-2 were used.

The three sections were first examined in CEREGE laboratory using optical microscopy. After identification of opaque inclusions, sections were then examined via secondary electron and backscattered electron (BSE) images using a HitachiS3000-N scanning electronic microscope (SEM), operated at 15 kV, equipped with a Bruker energy dispersive spectrometry (EDS) microanalysis system for *in-situ* chemical analyses. Phosphate-rich inclusions were identified in the silica-rich glass. Advanced imaging and EDS measurements were performed on the inclusions using a JEOL JSM-IT800SHL Field Emission Gun SEM with the Oxford Ultim Max 100mm^2 Silicon Drift Detector (SDD), a dwell time of 0.1 µs, a real-time of 15 to 45 min, and a resolution of 512x512 pixel was applied to various field of view depending on the inclusion diameter. BSE mosaics were acquired and assembled using Aztec® software.

Raman spectra were collected on the phosphate-rich inclusions using a Horiba micro-Raman LabRam HR800 evolution using a 532.31 nm excitation from DPSS laser and 1800 gr/mm (volume excitation of a few microns) at Laboratoire de Geology de Lyon (LGL) in Ecole Nationale Supérieur de Lyon (ENS de Lyon). Typical duration for each measurement was 1 to 2 min with >5 times repetition.

Seven electron-transparent lamellae (1 in ivorite, 4 in MN-AAT1, and 2 in MN-AAT2) targeting characteristic mineral inclusions were prepared using a Thermo Fisher Scientific FEI 125 Helios Nanolab 600i focused-ion beam scanning electron microscope (FIB/SEM) in MANUTECH USD platform in Saint-Etienne (France). Nanoscale characterization was performed at 200 kV with a NeoARM200F (scanning) transmission electron microscope (TEM/STEM), operated by the consortium Lyon Saint Étienne de Microscopie (CLYM) and hosted within the Hubert Curien Laboratory, Saint-Etienne (France). The NeoARM200F is equipped with a cold field-emission gun and a sixth-order aberration corrector (ASCOR). Images were obtained using Bright-field (BF, unscattered electrons) and Dark-field (DF, scattered electrons) detectors in TEM mode, both providing information about the mineral structure. A high angular dark field (HAADF) detector provides a chemical information with heavy material appearing brighter in the image, with an angle of detection usually between 50 and 150 mrad and up to 70 to 200 mrad, in STEM mode. A JEOL large angle silicon drift EDS detector (0.96 sr) was used to acquire X-ray maps with dwell time of 0.1 µs and a real time of 10 min to 1 h depending on the field of view and whether a quantification procedure was expected to be applied to the dataset. Quantification was achieved using the Cliff-Lorimer method (Cliff and Lorimer, 1975), an absorption correction procedure (Morris, 1980; Horita et al., 1987; Zanetta et al., 2021, 2022; Le Guillou et al., 2024) and using theoretical k-factors provided by JEOL®. Electron energy loss spectroscopy (EELS) was carried out using a Gatan Quantum spectrometer and provides a local information about the chemistry and oxidation state of a given element. Edges in energy arise from the ionization of the inner shell by the interaction of the electron beam with the sample. The convergence and collection semi-angles were 30 and 60 mrad respectively. The presented STEM-EELS dataset was acquired from a region of 2.7 × 3.2 µm^2, with a sampling of 50 × 60 pixels^2. Subpixel scanning (64 × 64) was employed. The dwell time was 0.1 s at a dispersion of 0.1 eV/pixel. The sample thickness in the regions of interest was evaluated to τ/λ = 0.4–0.6 (~50-70 nm) by Fourier-Log deconvolution on the low-loss EELS spectra (Iakoubovskii et al., 2008). All the multidimensional datasets (Raman, EDS, and EELS) were processed using Hyperspy library (de la Peña et al., 2022). EDS and EELS processing procedures are detailed in previous works (Zanetta et al., 2019, 2023; Noguchi et al., 2023).

3. Results

3.1. Bulk analyses (Magnetic susceptibility and ICPMS)

The magnetic susceptibility (χ) measured on MN-AATs and ivorites, is distributed in a very narrow range with a mean χ of 93 ± 10 and 116 ± 5 × 10^{-9} m^3 kg^{-1}, respectively (Rochette et al., 2019; Soro et al., 2023). Such a narrow distribution is typical of tektites as it indicates both the lack of Fe^{3+} and homogeneous iron content (Rochette et al., 2015). However, ICT showed a χ value of 55 × 10^{-9} m^3 kg^{-1}, the lowest ever measured for an ivorite. Accordingly, its FeO content is 3.69 wt% (Table 1) is lower than average of 6.16 wt% for ivorites (Koeberl et al., 1997). Comparison between χ and FeO content indicates negligible ferromagnetic impurities for ICT. On the other hand, MN-AAT shows a high χ values of 651 × 10^{-9} m^3 kg^{-1}, while the FeO content of MN-AAT is 4.15 % (i.e. in the range for a MN-AAT e.g., Table 1). Hysteresis measurement of MN-AAT confirms a significant ferromagnetic content with a saturation magnetization (M_s) of 69.5 mAmkg^{-1}. This is equivalent to a pure magnetite content of 800 ppm

ICP-AES measurements show that ICT is outside the published ivorite range for the following elements: ICT is enriched in Ca, Na, Si, and depleted in Fe, Ti, K (Table 1). Other major elements are in the range of previously measured ivorites. Concerning minor elements, ICT is characterized by a Sr excess, in line with Ca excess, and a Ce and Zr depletion with respect to typical ivorites. MN-AAT lies within the Australasite compositional range in terms of major elements, except for an excess in Na and Mn. MN-AAT is in the high range for Al, Ca, Fe and Mg, and shows a relatively low Si (Table 1). Concerning trace elements, the notable difference of MN-AAT with the composition from literature is its high Ba content, 569 ppm, compared to an average of 319 ppm (Amare and Koeberl, 2006), and its relatively high Ce and Zr content (Table 1).

MN-AAT is richer in Si and K than ICT (Table 1), and poorer in Na, Mg, Fe, Al. Overall, the only chemical similarity between ICT and MN-AAT is their high Na and Ca content with respect to average similar-type tektites. Phosphorus measurements on tektites are rare. P_2O_5 content of ICT is 0.07 wt%, above contents published by Cuttitta et al., (1972), with an average of 0.04 and a maximum of 0.06 wt%. MN-AAT has P_2O_5 content of 0.10 wt%, equal to the average for MN-AAT (Son and Koeberl, 2005). Both samples are also in the low range in Co, Ni, Cr (only Ni is reported in Table 1 as it is the most sensitive element to gauge extraterrestrial contamination, e.g. Folco et al., 2023). This suggests very minor extraterrestrial contamination, if any.

3.2. Microscopic characterizations (SEM and Raman)

The contrast in the BSE mosaic images clearly illustrate the chemical and textural heterogeneity of the two anomalous tektites (Fig. 1, see also optical images Fig. S1 and mosaic of MN-AAT2, Fig. S2). **ICT** contains vesicles (0.5 % of the surface of the section), and large-scale chemical variations evidenced by schlieren (flow bands of relatively high and low SiO_2 glass, e.g., Fig. 1a). The clear chemical foliation and the presence of mineral inclusions suggest that this sample is close to a Muong Nong-type. Lechatelierite domains (dark grey in BSE) contrast with the host glass (lighter grey) which contains heavier elements. We note that the contact between lechatelierite and felsic glass is unambiguous but diffuse in the BSE images, due to a slight change in composition over a few micrometers. Even if lechatelierite is often referred to as "grains", we prefer the term of domains as there is no well-defined interface between the lechatelierite and the host glass. **MN-AAT** glass also shows chemical variations on the micrometer scale (Fig. 1b). However, these variations are more diffuse and occur on a smaller scale than in ICT.

Table 1
Major and selected trace elements chemical composition of the tektite samples compared to previous ranges of concentrations. For ivorites: Cuttitta et al., (1972); Koeberl et al., (1997); for Muong Nong australasites: Koeberl (1992); Son and Koeberl (2005); Amare and Koeberl (2006).

Sample\Elmts	SiO_2	TiO_2	Al_2O_3	FeO	MnO	MgO	CaO	P_2O_5	Na_2O	K_2O	Sr	Ba	Zr	Ni	Ce
ICT	**69.5**	**0.48**	**16.4**	**3.69**	**0.04**	**3.62**	**2.33**	**0.07**	**2.64**	**1.13**	**507**	**434**	**88**	**27**	**30**
Ivorite range	66.2–69.1	0.54–0.61	15.8–17.1	6.03–6.80	0.04–0.07	2.64–4.39	0.71–1.61	0.03–0.6	1.53–2.44	1.7–2.13	170–390	260–520	90–195	94–260	35–49
average	67.1	0.59	16.74	6.16	0.06	3.46	1.38	0.04	1.9	1.95	260	374	134	180	42
MN-AAT 1	**77.09**	**0.61**	**11.74**	**4.15**	**0.15**	**1.72**	**1.49**	**0.1**	**1.33**	**2.33**	**117**	**569**	**394**	**27**	**90**
Australasite range (MN type)	74.3–80.8	0.49–0.78	8.57–12.5	3.11–4.63	0.05–0.12	1.22–2.35	1.18–2.01	0.07–0.11	0.96–1.15	2.16–2.47	98–160	204–349	287–414	29–86	65–88
average	78.9	0.63	10.18	3.74	0.08	1.43	1.21	0.1	0.92	2.42	136	341	280	55	61

Well-identified lechatelierite domains are rare in MN-AAT and more diffuse than in ICT. Residual Si-rich elongated domains probably represent diluted lechatelierite and suggest more advanced mixing with the host glass. A few large vesicles (100–500 μm) are distributed in the section (~1% of the surface). Foliation is marked by numerous schlieren (Fig. S3) and by lighter gray patches enriched in Fe, Al and Ca in the middle of the section (Fig. 1c). **Both ICT and MN-AAT** exhibit bright dense subspherical mineral inclusions (0.5–20 μm in diameter) embedded in the high silica glass. Raman spectra indicate that it is a relaxed silica glass (McMillan et al., 1994), with no indication of shock (Okuno et al., 1999). These inclusions will be named hereafter Ca-phosphate inclusions based on EDS analysis. ICT displays few inclusions clustered in two locations (Fig. 1 and Fig. 2) while MN-AAT exhibits numerous Ca-phosphate inclusions (Fig. 1 and Fig. 3) that are mainly embedded in filaments of a poorly mixed, brighter material (Fe-rich flow lines) than the host glass (Fig. 1d). A rough estimate of ~5 to 10 inclusions/mm^2 is obtained by thresholding the grayscale mosaic.

In ICT, Ca-phosphate inclusions (~1–4 μm in size) are systematically included in lechatelierite domains (Fig. 2a). According to EDS analysis and their homogeneous BSE contrast, they are single-phase inclusions (Fig. S4). Raman Ca-phosphate spectrum (Fig. 4a, green line) shows evidence of mixing with the surrounding glass (Fig. 4a, red line) but still exhibits well-identified double peak of merrillite with maximum at 967 and 951 cm^{-1} (Lafuente et al., 2015). Broad peaks are consistent with disordered phosphate (Pucéat et al., 2004). The Raman spectrum of the P-free glass consists of a broad structure from 300 to 650 cm^{-1} with a main peak at 453 cm^{-1} corresponding to the Si-O-Si bending a small peak around 784 cm^{-1} (motion of Si against its tetrahedral cage) and one broad band centered around 1000 cm^{-1} due to symmetrical stretching motions of the silica tetrahedra, whose intensity varies with the aluminum content (McMillan and Piriou, 1983; White and Minser, 1984).

MN-AAT shows a diversity of inclusions (Fig. 3, Fig. S5). They mostly consist of a single-phase Ca-phosphate inclusion (Fig. 3a). Numerous inclusions exhibit a rim of Si-rich glass depleted in heavy elements (P, Ca, Fe) that is surrounded by an aureole of glass containing phosphate nanospheres (Fig. 3a). Those phosphate nanospheres show a clear evolution in size, largest spheres are close to the inclusion, and spheres become smaller as one moves away from it (Fig. 3a). Some inclusions are embedded in lechatelierite (Fig. 3b). More complex phase assemblages are also observed among the inclusions of the MN-AAT (e.g., Fig. 3d, e, f and Fig. S5). Many of these are concentrated in schlieren choked with nanometric high-Z specks (emulsion texture, Fig. 3c). Four main phases have been identified (both in MN-AAT1 and MN-AAT2) in those peculiar mineral inclusions using Raman (Fig. 4) and EDS analyses (Fig. S6-S7). The largest inclusions frequently show the same sequence: a platinoid-rich nucleus (<50 nm, mostly enriched in Pt, Ru and Rh and with trace of Os and Ir, e.g., Fig. 3e and Fig. S8), a dendritic spinel that shows an enrichment in Al (replacing Fe) in the periphery of the grain (Fig. 3e, and Fig. S7). This assemblage is embedded in a pyroxene that is surrounded by a Ca-Mg-phosphate (Fig. 3d, e, f and Fig. S6, S7). Such sequence is not observed in smaller inclusions (<5 μm). Their observation may also depend on the section cut through the inclusions. Pyroxene Raman spectrum displays two peaks at 651 and 996 cm^{-1} and a small double peak at 310 and 348 cm^{-1} (Fig. 4b, yellow line). The peak frequencies at 651 and 996 cm^{-1} are lower than usually found in pyroxenes, likely due to a high-Fe content, and the peaks are broad, indicating significant disorder. The magnetite spectrum is characterized by a broad band from 450 to 750 cm^{-1} (Fig. 4b, blue line), also indicative of disorder. Phosphate Raman spectrum (Fig. 4b, green line) exhibit a characteristic single peak at 966 cm^{-1} which could be consistent with strongly disordered apatite (Pucéat et al., 2004). Raman spectrum of the host glass (Fig. 4b, red line) is relatively similar to ICT but show a more intense, broad peak at 1626 cm^{-1} might indicate minor Fe-oxide (maghemite) contribution (de Faria et al., 1997). Platy Ti-rich magnetite (<8 at%) is found cross cutting the mineral assemblage of the

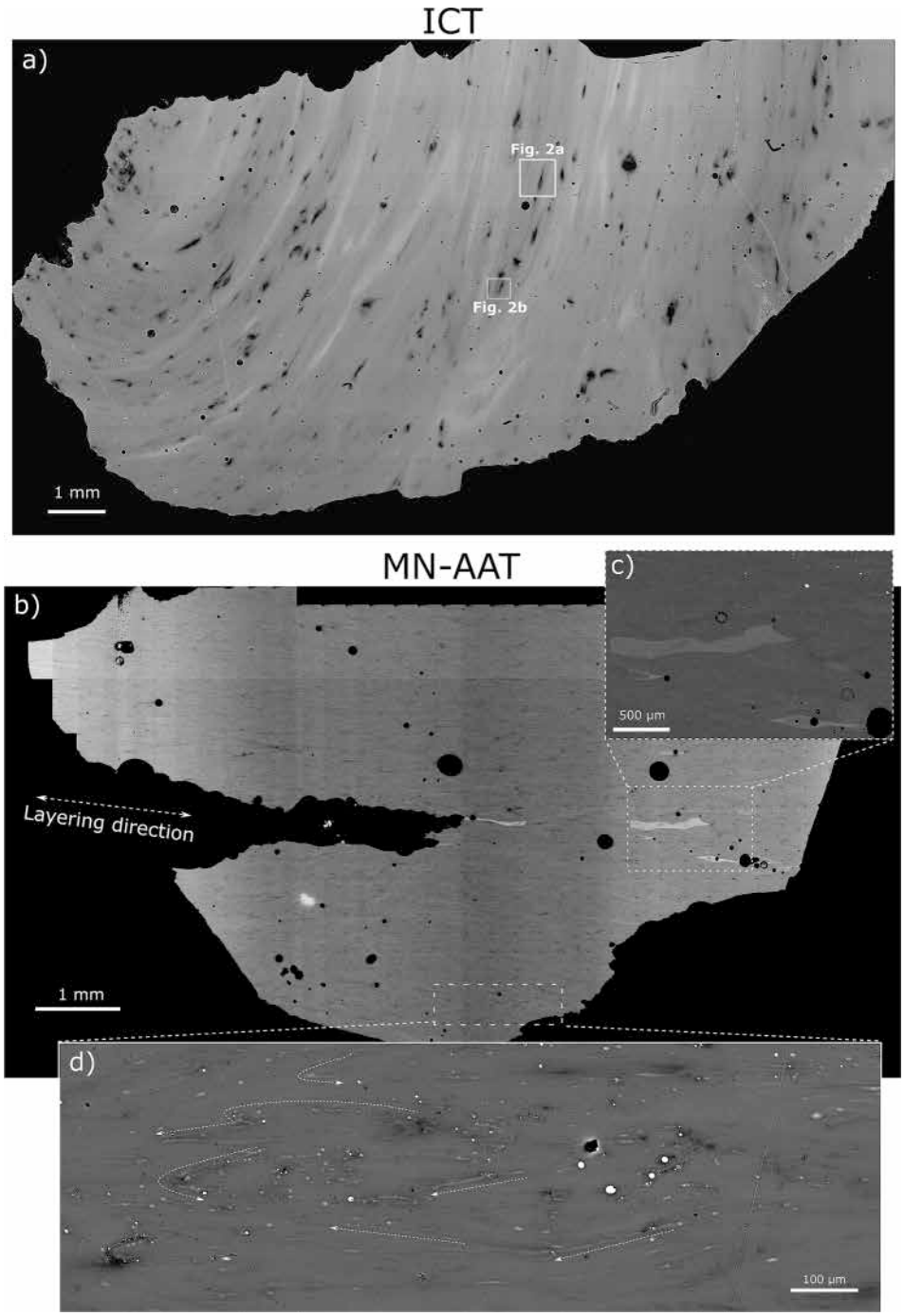

Fig. 1. Back-scattered electron image mosaics of the ICT and MN-AAT samples. ICT show a foliation highlighted by elongated lechatelierite grains (dark grey regions). Few vesicles are visible in the two mosaics. c) MN-AAT show a more homogeneous contrast but layering is visible in the middle of the section. d) MN-AAT is characterized by a high density of phosphate-rich inclusions. A particularly enriched area (in mineral inclusions) is shown by the selected field of view in the bottom of the mosaic. Inclusions are associated with Fe-rich flow lines (white arrows).

inclusion (Fig. 3f, Fig. S6). Depending on the orientation, the Ti-rich magnetite can be observed as needle (like whiskers) in SEM BSE images, but further TEM analysis showed a tabular geometry (e.g. Fig. 3d).

3.3. Nanometric characterizations (FIB/TEM)

At the nanoscale, the **ICT** Ca-phosphate inclusion (cf. Fig. 2 for location of the extracted lamellae) consists of two distinct phases (Fig. 5a, c) identified using selected area electron diffraction (SAED) patterns and EDS maps (Fig. 5b, d and Fig. S9). SAED patterns give information on crystal structure and orientation. The indexation of the SAED pattern shows that the crystalline phase (Fig. 5b) is merrillite, nominally, $Ca_9Na[Fe,Mg][PO4]_7$, the anhydrous end-member of the merrillite–whitlockite solid solution series. The phosphate composition is not in a stoichiometric ratio, which may indicate the presence of (OH–) radicals (i.e., the whitlockite pole). However, due to the inherent limitations of EDS quantification of cations, it is challenging to definitively ascertain the presence of OH-radicals or to provide a precise estimate of their quantity. It is embedded in a Ca-amorphous phosphate of a comparable composition (Fig. 5d, Table 2). Crystals of merrillite are acicular and show various orientations as demonstrated by diffraction contrasts varying from black to light grey in BF-TEM (Fig. 5a). The

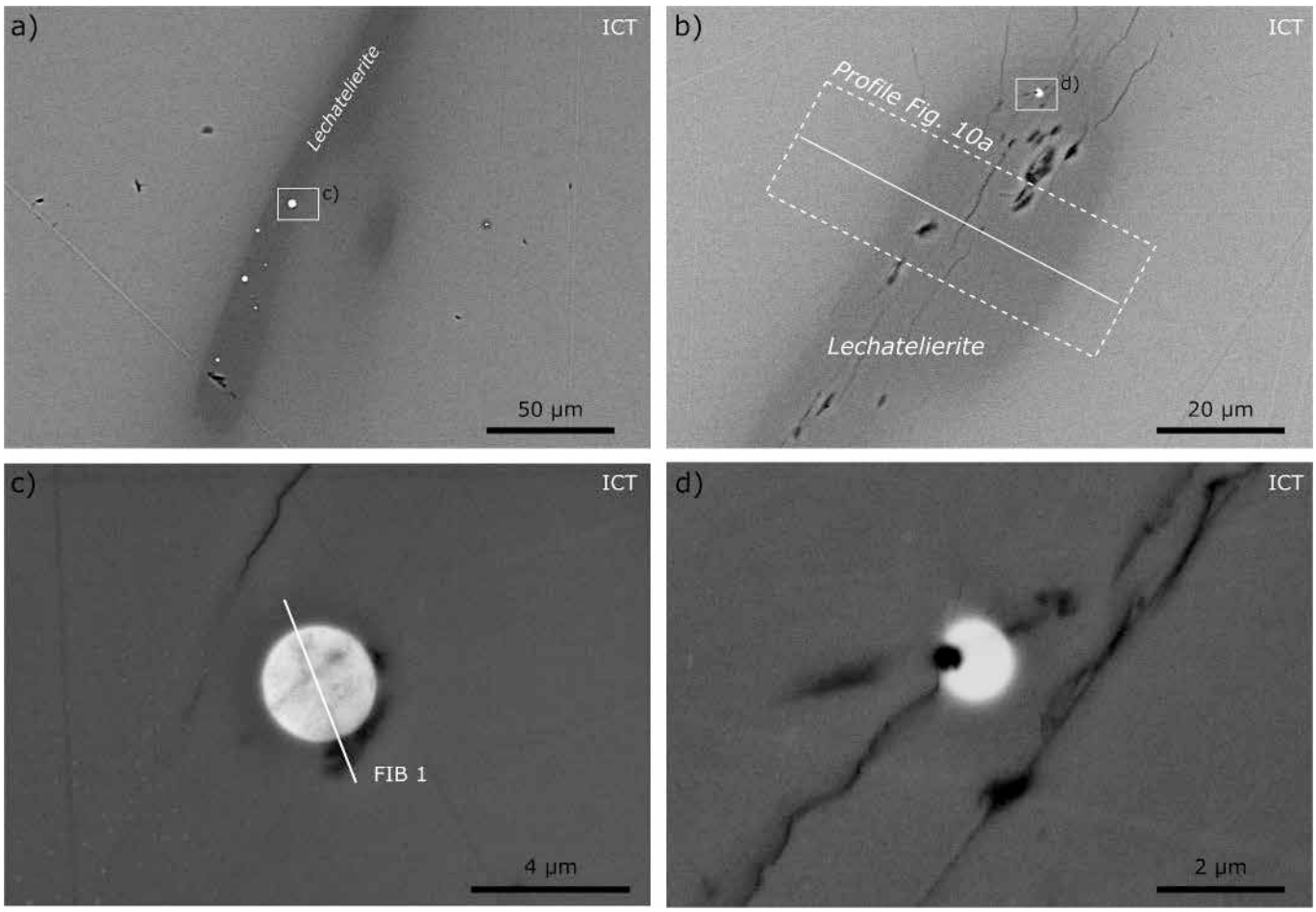

Fig. 2. Back-scattered electron images of Ca-phosphate inclusions in ICT. a) Lechatelierite with diffuse boundaries enclosing several phosphate-rich inclusions in ICT. b) Second region of interest with lechatelierite containing a single phosphate-rich inclusion. The white line indicates the EDS chemical profile shown in Fig. 10. The dashed rectangle indicates the pixel summed orthogonally to the profile to improve the signal-to-noise ratio. c) Phosphate-rich inclusion sampled for nanoscale analyses by TEM. The phosphate inclusion is homogeneous in BSE contrast. d) Smaller phosphate inclusion in the second region of interest. The dark spot is due to porosity.

STEM-EDS quantification shows a relatively high content of Mg (1.48 cation per formula unit, Table 2). BF-TEM images reveal dark nanospherules dispersed in the host glass that surround the phosphate-rich inclusions in ICT (Fig. 6a-b). Spherules show slight enrichment in P, Si and Ca (Fig. 6b and Fig. S10). Their size varies from ~150 nm to <5 nm as they approach the Ca-phosphate inclusion. All the dark inclusions in the glass are amorphous (Fig. 6c). The same spherules are observed in the host glass in MN-AAT in the vicinity of the inclusion (Fig. 7a-c

Several phases are identified from TEM/STEM-EDS and SAED analysis in the Ca-phosphate inclusion in **MN-AAT** (Fig. 7). Ca-phosphate contains Fe and Mg (and potentially F and Cl, with a low concentration of less than 0.1 at%, as indicated in Table 3), its selected-area electron diffraction (SAED) pattern closely matches that of apatite (Figs. 7a-d) and excludes that of panethite. The phosphate composition does not provide a neutral charge either, which may indicate the presence of (OH–) radicals or a disordered oxyapatite structure (Bulina et al., 2023). Pyroxene (Fig. 7f) is rich in Fe, Mg and Al (Table 3). The Al is distributed between the silica tetrahedral site and the metal site according to stoichiometric calculations. The mineral that appears as a needle in BSE images (Fig. 3d) is a non-stochiometric platy-shaped magnetite rich in Al and Ti (Fig. 7a, b, Fig. 8, Table 3 and Fig. S11). The magnetite shows long-range alternations (2–10 nm) of Al-rich and Ti-rich intergrowths (Fig. 8c, d and Fig. S12). Such intergrowths alter the magnetite diffraction pattern (Fig. 8b). The large spacing of the superlattice in real space results in small spacing of the superlattice reflections in the SAED pattern (diffraction spots distance <1 nm^{-1}). The atomic arrangement shows intergrowth of the Fe-rich and Al-rich domains accommodated by two distinct structures (Fig. 8c and d). Identification of the atomic arrangement reveals the intergrowth of magnetite in the [1 1 1] direction and corundum in the [−1 1 1] direction (Fig. 8d).

Dendritic Al-Fe spinels are characteristics of the complex inclusions found in the **MN-AAT** (Fig. 9). The branches near the nucleus extend and widen to form a broad, flat shape at the end of the hemisphere (Fig. 9a). Observation of numerous mineral inclusions in MN-AAT1 and MN-AAT2 shows that the spinel starts from the outer boundary of the mineral inclusion, systematically from a Pt-rich nucleus (see Fig. 3e), and grows towards the interior of the inclusion. The dendritic spinel shows a strong chemical variation in Fe from core to rim (Fig. 9b and Table 3). These chemical variations are accompanied by a variation in Fe oxidation state based on EELS measurements on the Fe $L_{2,3}$ ionization edge. The $Fe^{3+}/\sum Fe$ map show that the core is enriched in Fe^{3+} whereas the branch tips are richer in Al^{3+} and depleted in Fe^{3+}. The Al^{3+} is replacing the Fe^{3+} in the structure and most of the Fe is Fe^{2+} in the platy spinel.

3.4. *Quantitative estimation of temperature/heating duration from lechatelierite domains*

A recent study from Macris et al., (2018) quantitatively evaluated the heating duration of a tektite sample. In their study they used the diffusion profile located at the boundary between a lechatelierite grain and

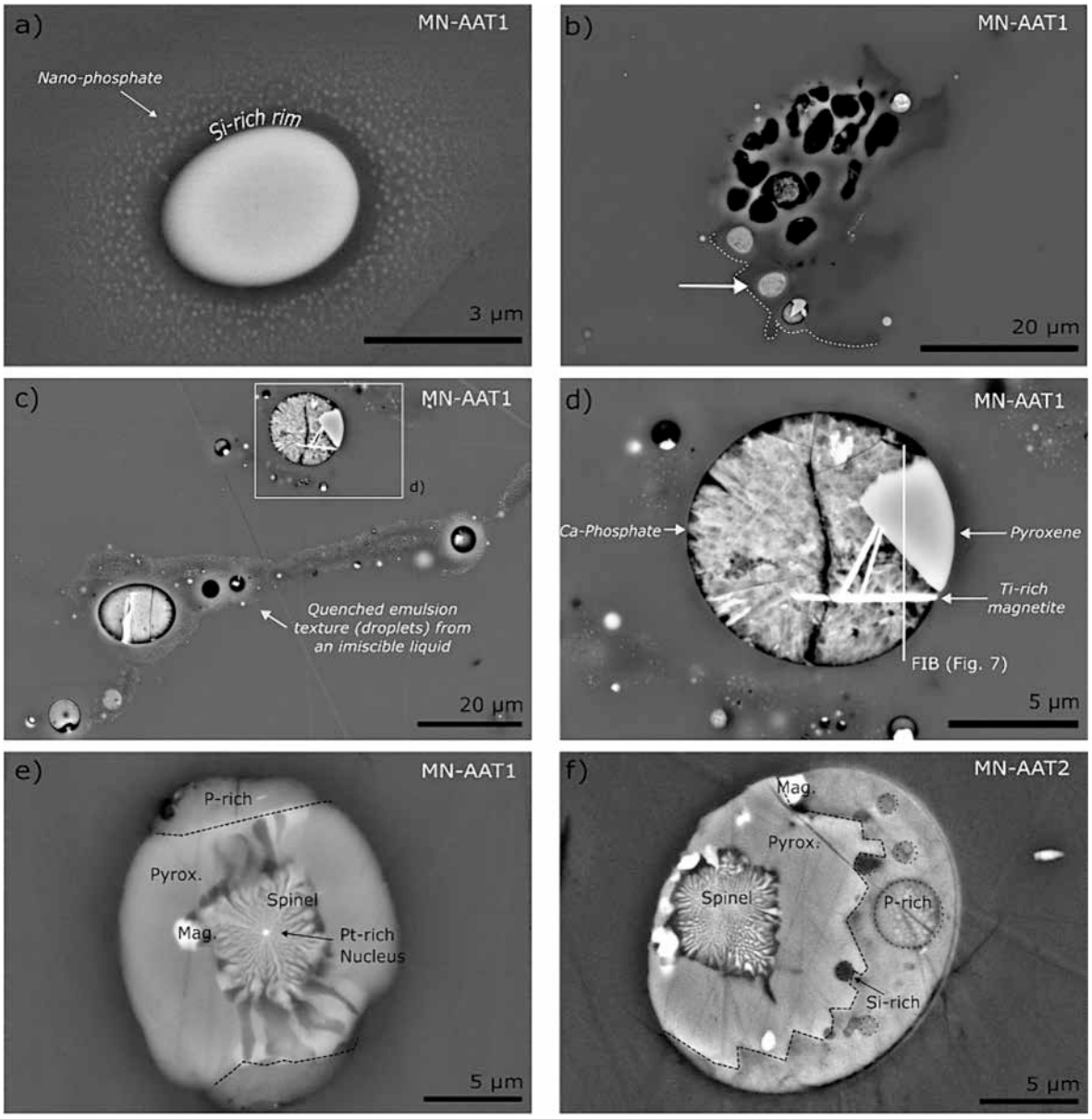

Fig. 3. Back-scattered electron images of phosphate-rich inclusions in MN-AAT (see also Fig. S5). a) A single-phase phosphate-rich inclusion in the MN-AAT section. Most inclusions appear homogeneous and single-phased. A ring of Si-rich glass surrounds the inclusion. Ca-phosphate nano-spheres also mantle the inclusion. The larger spheres are closer to the inclusion. b) Multi-phase inclusions embedded in lechatelierite (white arrow). Lechatelierite frothy texture is due to the high density of vesicles resulting from decompression. c) Complex multi-phase inclusions embedded in a SiO_2-rich flow band mixed with phosphate nanospheres. d) BSE image of a representative inclusion in MN-AAT (Fig. S6). Several phases are visible. The change in volume due to the crystallization of the minerals is marked by dark and empty areas. Localization of the FIB section is indicated. e-f) Recurrent mineral assemblage observed in phosphate-rich inclusion (Fig. S7). A Pt-Ru-rich nucleus facilitated the crystallization of a spinel which is enclosed by a pyroxene and a phosphate phase (Fig. S8). P-rich = Phosphate riche phase, Pyrox. = pyroxene, Mag. = Magnetite.

its host glass. They estimated the time needed to produce the observed chemical profile while the tektite remained in an isothermal impact vapor plume after fast heating and before quenching below glass transition temperature (in an order of few seconds to 600 s depending on the temperature). To achieve such estimation, Macris et al., (2018) first defined a simple relationship to calculate the profile length between SiO_2 (lechatelierite) diffusion in host glass as a function of time at a given temperature:

$$x = \sqrt{7.91Dt} \quad (1)$$

where x is the diffusion profile distance, D is the averaged diffusion coefficient at a given temperature, and t is time. Macris et al., (2018) also established the diffusion coefficient of lechatelierite in glasses with compositions close to tektites for temperatures ranging from 1800 °C to 2400 °C through experimental studies. To illustrate the use of their equations with a quantitative example, consider an interface analogous to MN-AAT, wherein SiO_2 varies from 100% to 70% from lechatelierite to host glass, and the temperature is 2000 °C. The value of $\ln D_{SiO_2\ 100\text{-}70\ wt\%}$ (m^2/s) is −28.3 (Fig. S13). Consequently, in order to produce a 20 µm diffusion profile at this temperature and with this chemical variation (70–100%), it would take 17.2 s. Their isothermal model is applied to quantify the diffusion profile observed in **ICT** and **MN-AAT** (Fig. 10). The two tektites show distinct chemical heterogeneities in the glass (Fig. 1). ICT shows diffuse but distinguishable lechatelierite domains (Fig. 2). MN-AAT shows evidence of a stronger mixing and potentially a more advanced diffusion (Fig. 1 and Fig. S3). Most of the lechatelierite domains significantly expanded in the MN-AAT glass (Fig. 1) and only

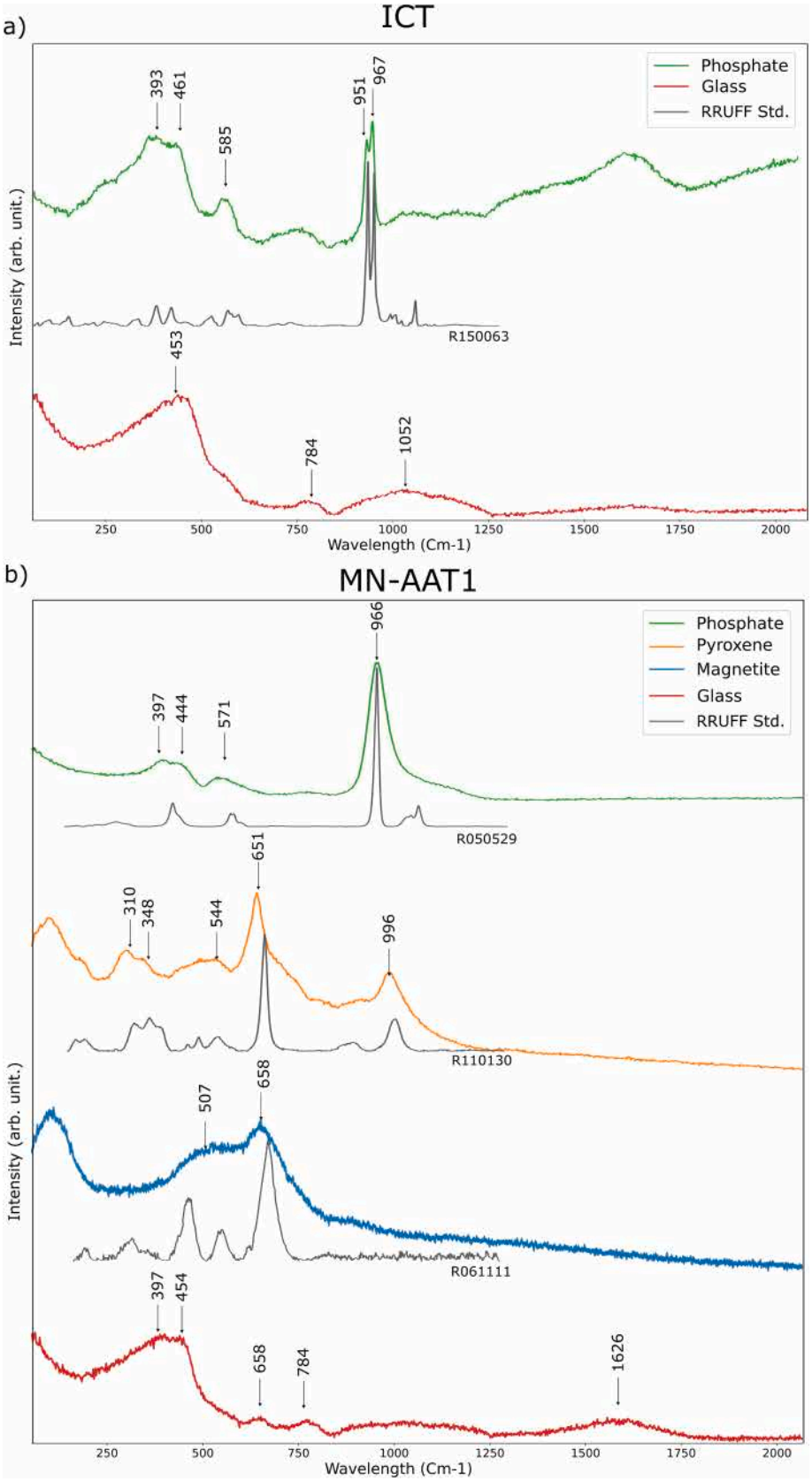

Fig. 4. Raman spectra of the different phases observed in ICT and MN-AAT. a) Spectra of the phosphate inclusion and the P-free glass in ICT. b) Spectra of the main four phases observed in the complex inclusions (≥5 μm) of MN-AAT. RRUFF reference spectra are compared to experimental data.

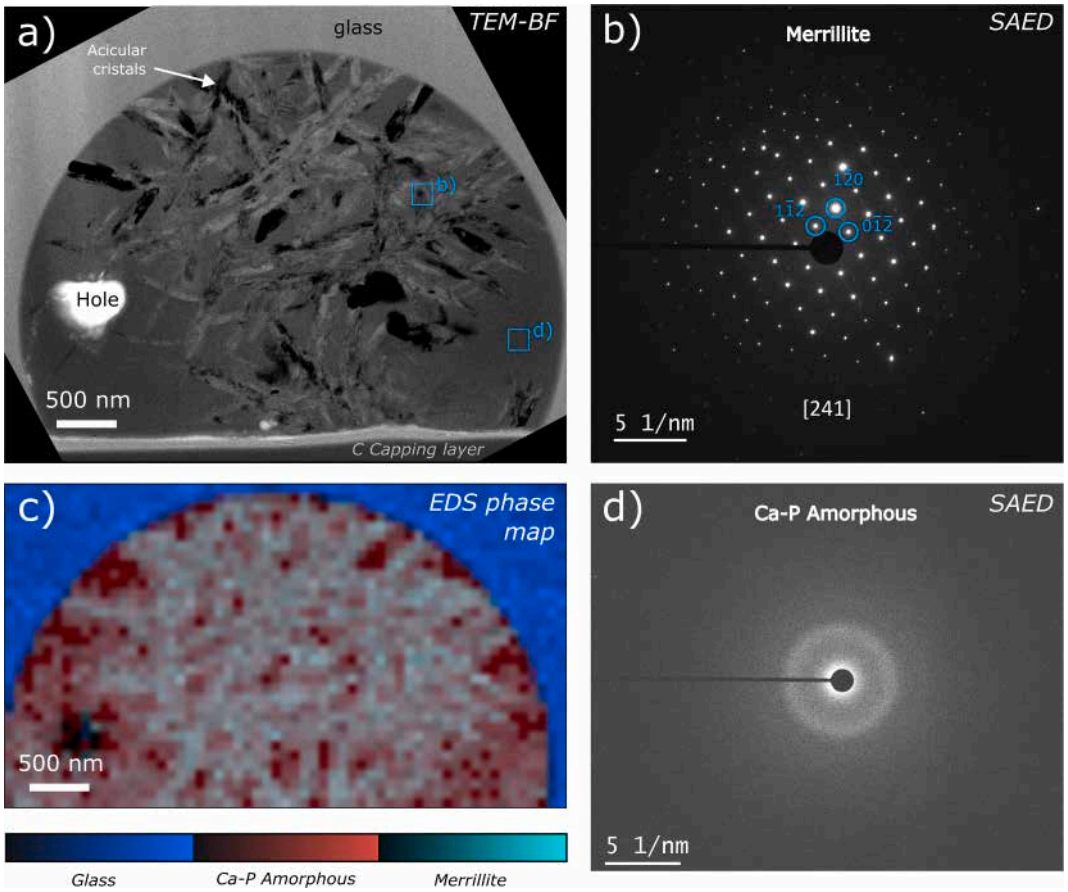

Fig. 5. TEM analyses of the phosphate-rich inclusion in the ICT. a) Bright field TEM image of the well-rounded inclusion. Acicular crystals are embedded in a smooth and homogeneous phase, i.e., amorphous P-rich glass. b) Selected area electron diffraction (SAED) pattern of the merrillite phase oriented along the [2,4,1] direction. c) Phase map based on the STEM-EDS spectrum image and obtained from linear mixing of reference spectra (Fig. S9). d) SAED pattern of the amorphous phase embedding the merrillite crystals.

Table 2
STEM EDS quantification (At%) of the two phases observed in the ICT inclusion. The phosphate may contain traces of molecular OH in its formula, but these radicals could not be detected by EDS quantification.

	Atomic %												
	O	Si	Al	Mg	Fe	Ca	P	Ti	Cr	Mn	K	Na	Cl
Amorphous	59.16	0.397	0.05	2.553	1.282	18.716	16.233	0.119	0.129	0.139	0.139	0.924	0.159
Merrilite	60.673	0.506	0.152	3.216	1.871	16.25	15.269	0.172	0.162	0.162	0.172	1.203	0.192
	Formula unit												
	O	Si	Al	Mg	Fe	Ca	P	Ti	Cr	Mn	K	Na	Cl
Merrilite	28	0.23	0.07	1.48	0.86	7.5	7.05	0.08	0.07	0.07	0.08	0.56	0.09

two domains could be used to establish a characteristic diffusion profile (Fig. S3). Application of an averaged diffusion coefficient $\ln D_{SiO_2\ 100\text{-}68\ wt\%}$ and $\ln D_{SiO_2\ 100\text{-}77\ wt\%}$ (equation (1)) to the SiO_2 profiles extracted from the two tektites (Fig. 10) yields heating durations of 4 and 6 s at 2400 °C and 725 and 1245 s at 1800 °C respectively (Fig. S13). As specified by Macris et al., (2018), characteristic diffusion times within lechatelierite are dependent of the concentration of SiO_2 in the host glass Lechatelierite diffuses and equilibrates faster for lower SiO_2 concentration (Fig. S13: yellow for **ICT** vs green line for **MN-AAT**).

From their experiments Macris et al. (2018) established a function to estimate the diffusion coefficient at various SiO_2 concentrations and temperatures:

$$lnD_{SiO_2} = -0.12W - \frac{48605(\pm 5019)}{T} + 3.23(\pm 2.14) \quad (2)$$

where D is diffusion coefficient in m^2/s, W is the concentration of SiO_2 (wt.%) and T is temperature (K). The diffusion time and length can be modelled for varying heating duration and temperatures using this equation accounting for the dependency of the diffusion coefficient with SiO_2 concentration (Fig. 11 and Fig. 12). For a given temperature and diffusion time, the diffusion distance is calculated for each composition. This means that at each point a new composition-dependent diffusion coefficient is calculated. The next diffusion distance is then calculated for a different composition. The mean profile distances are comparable in ICT and MN-AAT, with a value of approximately 20 μm. However, MN-AAT displays a higher SiO_2 content (77 wt w%) in the host glass in

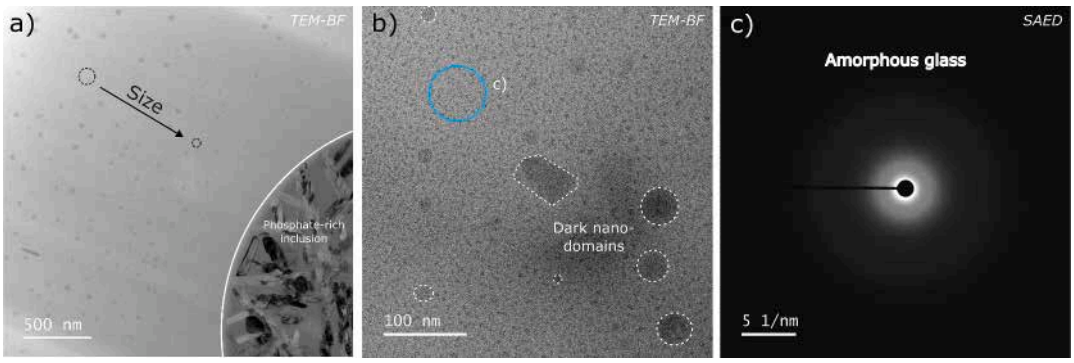

Fig. 6. Bright field TEM images and SAED pattern of the glassy material surrounding the inclusion in ICT (cf. Fig. 5). a) Dark nano-domains are dispersed in the host glass. The size of the domains decreases (100 nm to <5 nm) toward the direction of the inclusion (see annotations). b) Most of the dark inclusions are circular but some are elongated or rectangular. Domains contain heavier elements (Ca, Fe and Mg) than the host SiO_2-rich glass (Fig. S10). c) SAED pattern of the amorphous nanodomains.

comparison to ICT (68 wt%). In order to reproduce the same profile distance in MN-AAT, a higher peak temperature or an extended heating period is necessary due to the higher SiO_2 content, which limits the diffusion from the lechatelerite to the host glass (Fig. S13).

MN-AAT also shows domains of Fe-rich glass with sharp boundaries (Fig. 1). Sharp boundaries are unexpected in view of the chemical heterogeneity of the glass and the diffuse nature of lechatelierite domains (Fig. 1). To reconcile these two observations, we propose that the Fe-rich glass (also enriched in Al and P) originated from a late addition of material in the glass. Addition of material into the glass may have happened later due to higher melting temperatures of the material at its origin. The late addition of refractory elements has potentially been followed by a rapid quenching that limit the diffusion and preserves the well-marked boundaries of those areas within the host glass.

4. Discussion

4.1. Various thermal history recorded in tektites

(a) Temperature and heating duration

Tektites have recorded variable thermal histories because of 1) the different kinetic energy and momentum (or mass and speed) of the impactor generating each strewn field but also 2) the location of the source material (depth and distance to impact) and 3) the various trajectories of samples following ejection (Barnes, 1961; Stöffler et al., 2002; Cavosie, 2018; Rochette et al., 2018). Qualitative and quantitative information on their process of formation may be inferred from the micro and nano-characterization of mineral inclusions. For instance, lechatelierite domains observed in tektites are often elongated and contorted, and show diffuse contact with the enclosing glass indicating high temperature of at least 1600-1700 °C to melt pure SiO_2 (e.g., Barnes, 1958; Glass, 1990; Wilding et al., 1996; French, 1998; Howard, 2011; Schaller et al., 2016). Tektites also have a low water content, which is typically explained by volatile loss at high temperature (Koeberl, 1992; Giuli, 2017). However, previous work on moderately volatile elements (Cu, K) indicated that isotopic ratios are typically identical to those observed in the upper terrestrial crust, exhibiting no isotopic fractionation (Humayun and Koeberl, 2004; Moynier et al., 2010). Even if quantitative estimates are scarce, it is widely accepted that tektites have been rapidly heated within seconds to temperature above 1800 °C to form lechatelierite and lose of most volatile elements, then quickly cooled over a few minutes to avoid the chemical homogenization of the glass and avoid the isotopic fractionation (Glass, 1990; Wilding et al., 1996; Macris et al., 2018).

Diffusion profiles from lechatelierite domains quantitatively demonstrate that MN-AAT was heated to a higher temperature or for a longer time than ICT (Fig. 11 vs Fig. 12). Within the different tektite fields, tektites retained their moderate volatile elements to a greater or lesser extent (Žák et al., 2012; Jiang et al., 2019). It has been shown that Muong Nong is one of the tektite groups that is the least depleted in volatile elements (notably when compared to ivorites), which would tend to indicate lower peak temperature than other tektites, or shorter heating time, or both. For example, an MN-AAT analyzed by Creech et al., (2019) showed small Sn depletion and Sn isotope fractionation. They attributed these results as being due to the proximity of the sample to the source and concluded that Muong Nong sample experienced shorter heating times at high temperatures than other groups. The loss of volatiles is also dependent of the diffusion coefficient within the sample. MN tektites can be considerably larger than the other tektite types, a factor that may also limit the loss of their volatiles.

Ideally, one would like to be able to constrain the peak temperature or the duration of heating (Figs. 11 and 12) to quantitatively estimate the thermal history of samples such as ICT or MN-AAT. However, most physical properties which can effectively describe the rheological behavior of a glass, such as viscosity, are generally dependent on temperature, duration of deformation and composition. In contrast, the viscosity ratio λ, of two materials is primarily dependent on temperature, once the composition is known. The deformation of lechatelierite (~100% SiO_2) droplets in a host glass (~75% SiO_2) depends on the viscosity difference between the two materials (i.e., the viscosity ratio $\lambda=\mu_{SiO_2}/\mu_{glass}$). If they are far apart, one of them will stretch strongly in a few seconds, while the other will be too viscous and behaves like a solid on such a short timescale (e.g., Taylor, 1934, Manga, 1996a). Manga (1996b) showed that for a viscosity ratio $\lambda > 4$, simple shear cannot stretch inclusions, whereas at low viscosity ratio $\lambda \leq 1$ they are rapidly stretched. In chaotic flows, the viscosity ratio may be higher (than 4) and yet lead to deformation of such heterogeneities, but the difference between the two viscosities cannot be too high (Stone, 1994; Mukherjee and Sarkar, 2009). In the case of lechatelierite and the host glass, the viscosity ratio can reach several orders of magnitude (Fig. 13a) over a wide range of temperatures (Richet, 1984; Toplis et al., 1997; Giordano and Dingwell, 2003). High temperatures (>2200 °C) are required to obtain low viscosity ratios (Fig. 13a). Thus, the tektites studied here have reached temperatures higher than 2200 °C for a short period of time. These characteristic times are of the order of seconds rather than minutes as it is often presumed (Wilding et al., 1996; Stöffler et al., 2002). Because MN-AAT is richer in SiO_2 than ICT, it requires higher heating temperatures or longer heating times to produce similar diffusion profile. On the other hand, this higher SiO_2 content may require slightly lower temperatures to produce viscosity ratios (μ_{SiO_2}/μ_{glass}) closer to 1 and allow for the stretching of lechatelierite domains (Fig. 13).

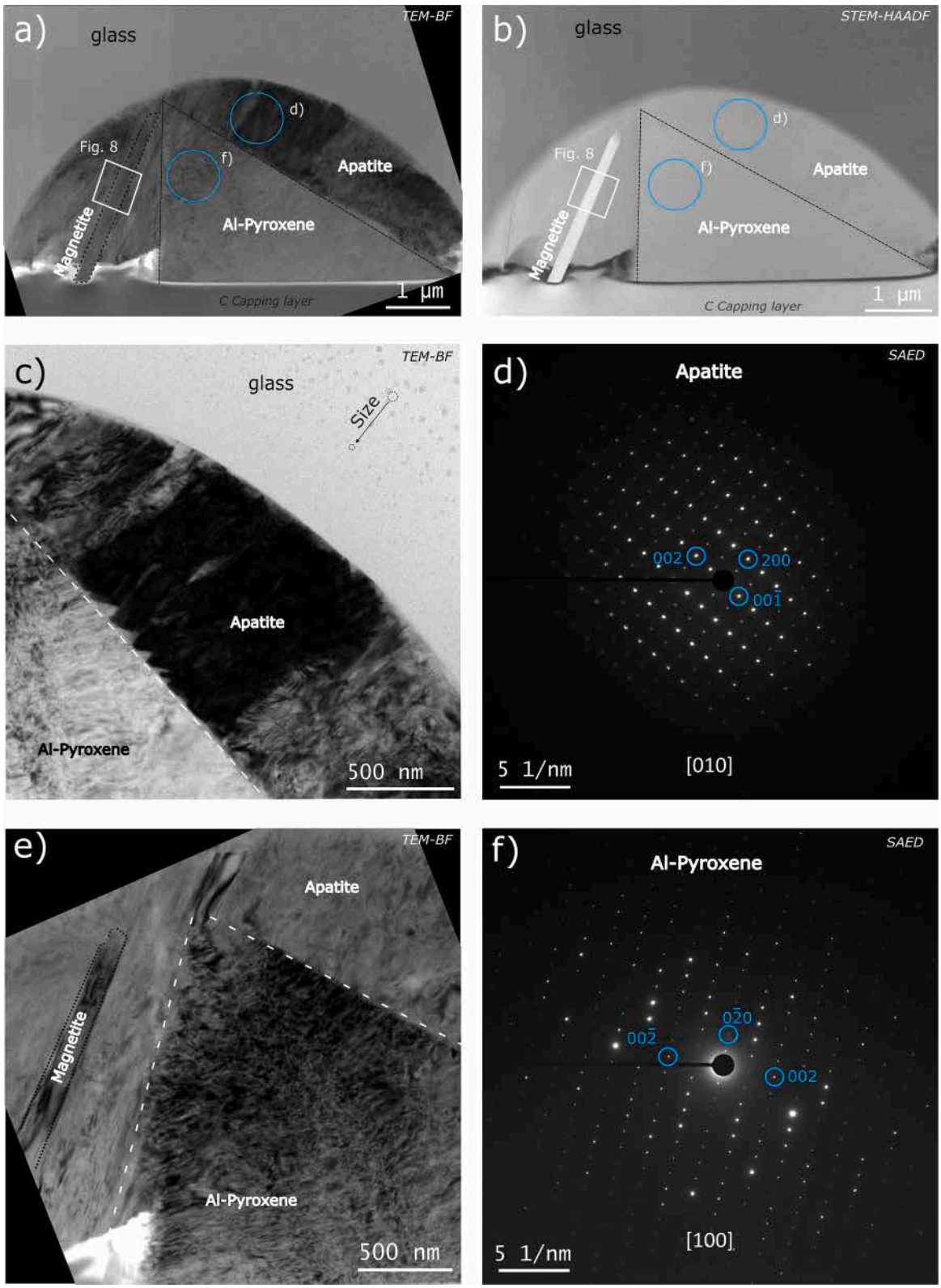

Fig. 7. TEM/STEM analysis of a phosphate-rich inclusion in MN-AAT1. a) Conventional BF-TEM image of the whole inclusion. Several phases can be identified and their boundaries are drawn using Bragg contrasts (mineral close to Bragg conditions for diffraction appear darker). b) STEM-HAADF image of the whole inclusion evidencing the platy magnetite. Magnetite and pyroxene are included in the phosphate (Fig. S11). c) BF-TEM image of the Ca-phosphate mineral (apatite). Diffraction contrasts show significant disorder in the crystal. Nano-domains of heavy material (Ca, Fe, Mg) are also observed in the silica-rich host glass surrounding the inclusion (Fig. 6 and Fig. S10). The evolution in size is similar to the nano-domains observed around the inclusion in ICT (Fig. 6). d) SAED allowing the identification of the phosphate phase as apatite oriented along the [0,1,0] direction. e) BF-TEM image of the Al-pyroxene. The boundaries of the crystal are sharp, but Bragg contrasts also evidence disorder in the crystal. f) SAED pattern allowing the identification of the pyroxene structure. The grain is oriented along the [1,0,0] axis.

Table 3
STEM EDS quantification (At%) of the five main phases observed in the MN-AAT1 inclusion. The magnetite is not stoichiometric due to the abundant substitutions in its structure (see Fig. 8). The phosphate may contain traces of molecular OH in its formula, but these radicals could not be detected by EDS quantification.

	Atomic %												
	O	Si	Al	Mg	Fe	Ca	P	Ti	Cr	Mn	K	Na	Cl
Glass	63.35	28.43	3.44	1.02	0.52	0.41	0.42	0.13	0.07	0.08	0.73	1.26	0.14
Fe/Mg Phosphate	59.26	1.03	0.78	10.16	4.44	7.59	15.07	0.16	0	0.25	0	1	0.25
Magnetite needle	54.22	2.32	8.23	4.44	20.04	0.39	3.1	4.02	0.27	0.29	0.31	1.92	0.45
Pyroxene	59.61	14.07	6.29	12.81	5.65	0.39	0	0.57	0.12	0.05	0.16	0.03	0.25
Fe/Mg Spinel	55.31	1.07	21.87	7.95	10.14	0.29	0.62	1.58	0.29	0.32	0.31	0	0.24
	Formula Unit												
	O	Si	Al	Mg	Fe	Ca	P	Ti	Cr	Mn	K	Na	Cl
Fe/Mg Phosphate	12	0.21	0.16	2.06	0.9	1.54	3.05	0.03	0	0.05	0	0.2	0.05
Pyroxene	6	1.42	0.63	1.29	0.57	0.04	0	0.06	0.01	0.01	0.02	0	0.03
Fe/Mg Spinel	4	0.08	1.58	0.58	0.73	0.02	0.04	0.11	0.02	0.02	0.02	0.00	0.02

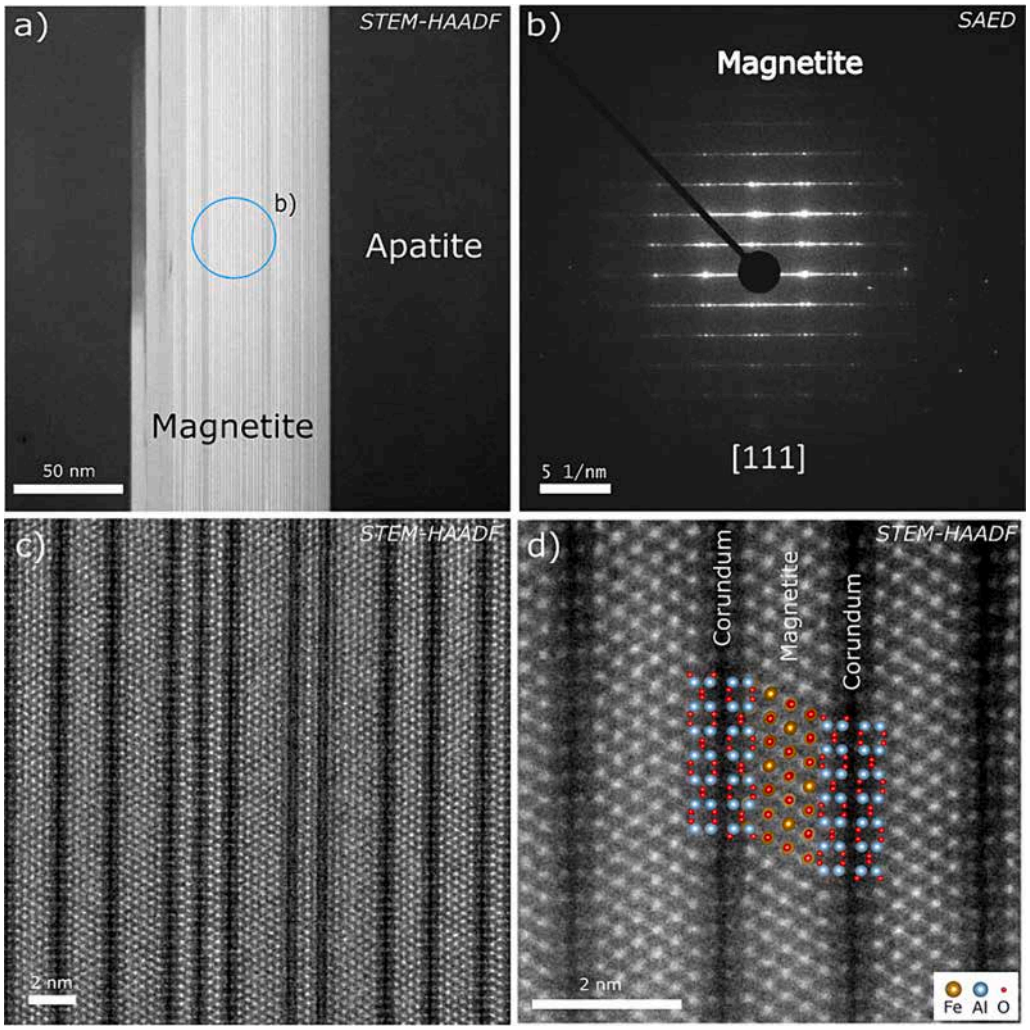

Fig. 8. Intergrowth of Ti-rich magnetite and corundum in phosphate-rich inclusion in MN-AAT1 sample (see also Fig. S12). a) Large field of view HAADF image of the platy magnetite observed in the [1,1,1] direction. b) SAED pattern of the magnetite showing superlattice reflection. c) Intergrowth of corundum (darker) and magnetite (brighter) domains. The dominant phase is magnetite that is in places replaced by corundum. d) Determination of the atomic arrangement of the magnetite-corundum intergrowth.

(b) Cooling rates

In MN-AAT complex inclusions, the sequential crystallization carries crucial information on cooling rates (crystallization of dendritic spinel on platinoid-rich nuclei, followed by the pyroxene crystallization and finally phosphate formation in late crystallization). Each mineral recorded a different stage of cooling. Under atmospheric pressure, spinel crystallizes at higher temperature (>1400 °C) than pyroxene (~900–1100 °C) and apatite (<1000 °C). The dendritic nature of spinel and the magnetite-corundum intergrowth (Fig. 8) indicate rapid

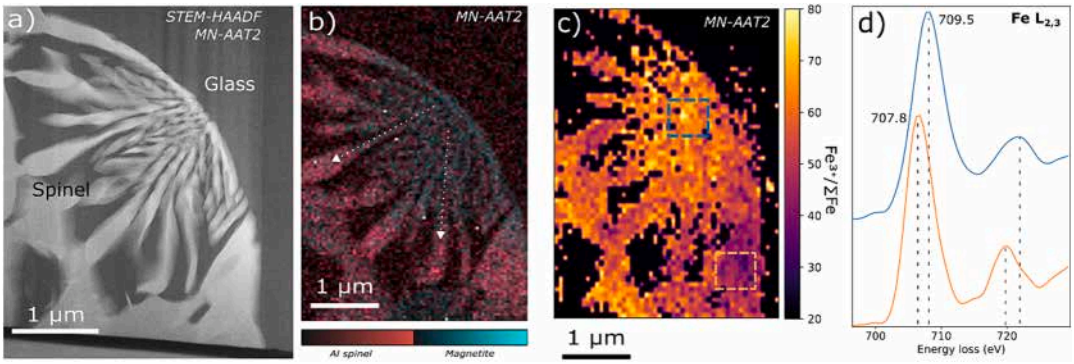

Fig. 9. Map of the chemical variation in the system Al_2O_3-Fe_2O_3-Fe_3O_4. a) HAADF image of a dendritic spinel in MN-AAT2. b) Phase map of Al-spinel and Fe-spinel (i.e., closer to a magnetite endmember). Shade in color allow to represent chemical variations. c) Map of the $Fe^{3+}/\sum Fe$ variation in the dendritic spinel from MN-AAT2 based on EELS $L_{2,3}$ calibrations. d) Spectra showing the Fe $L_{2,3}$ chemical shift in energy between the core and the edge of the spinel and evidencing the Fe oxidation state variation during the crystallization of the mineral.

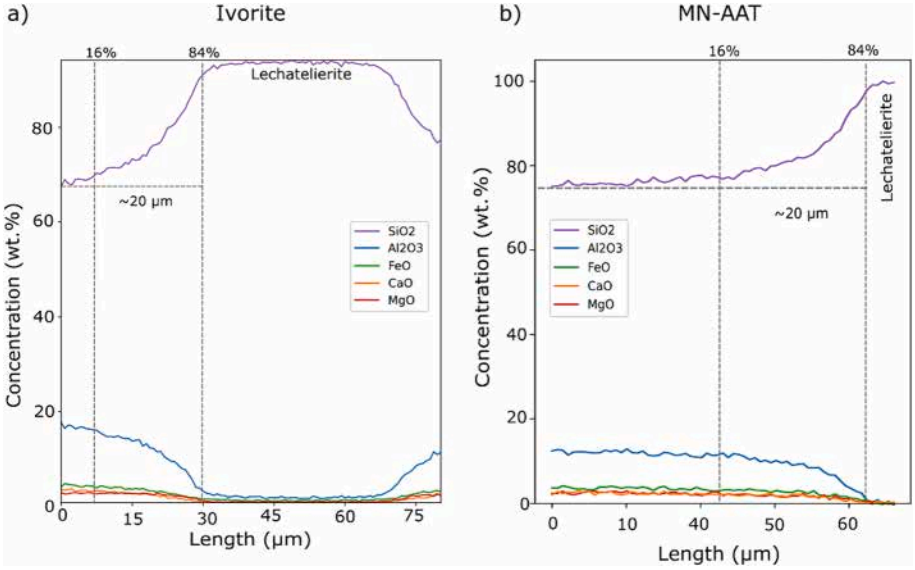

Fig. 10. SEM-EDS profiles. a) profile extracted in ICT from the lechatelierite domain in Fig. 2b. b) Averaged profile extracted in MN-AAT1, see Fig. S3. All elemental profiles (Al_2O_3) are approximately of the same length as SiO_2 except MgO which show a shorter profile (16.5 µm). The profile length is defined by using the 84–16 % composition rule (composition difference between the two plateaus in Fig. 10) described in Macris et al., (2018). It has the advantage of using a large portion of the profile while avoiding the nearly flat parts that may be difficult to model.

crystallization and fast cooling rate at high temperature. Conversely, the well-crystallized structure of the pyroxene and phosphate mineral indicate slower cooling rates for lower crystallization temperature. This observation indicates an evolution of cooling rates as a function of temperature for MN-AAT, with fast cooling rates at high temperatures forming dendritic crystals and lower cooling rates as cooling proceeds favoring the complete crystallization of the inclusions (Fig. 13). **In ICT,** there is no crystallization sequence, and only the presence of merrilite can provide information on cooling rates. Apatite and merrillite–-whitlockite are common minerals in many plutonic rocks and extra-terrestrial bodies and coexist in similar temperature and pressure conditions (McCubbin et al., 2014; Słaby et al., 2017). The occurrence of one phase over another is not dependent of the temperature but is rather related to the Ca content that is higher in the ivorite sample (Table 1). However, their nanostructure is characteristic of their cooling rates. The amorphous phosphate surrounding the merrillite crystals in the ICT (Fig. 5) indicates faster cooling rate than MN-AAT which, in contrast, exhibits completely crystallized inclusions (Fig. 7).

Cooling rates can also be estimated from the density of inclusions that nucleated in tektites (Fig. 1d, Fig. 2). Solid phases cannot nucleate in a liquid that is cooled too rapidly. Estimated rates also depend on the bulk composition since glass with higher SiO_2 content would require lower cooling rates to start crystallizing isolated crystals (Lofgren and Hargraves, 1980; Zhang, 2009). The glass forming ability of silicate melts with composition close to tektites has previously been investigated (Vetere et al., 2015). To obtain textures and percentages of isolated inclusions similar to those in natural glass (Fig. 2), cooling rates for ICT must have exceeded of 2000 °C/h (cooling duration = 1 h). Those results are in the range of cooling rates estimated by calorimetric relaxation geospeedometry (1–10 °C/s, i.e., 3 to 30 min e.g., Wilding et al., 1996). Because MN-AAT has a higher inclusion density (Fig. 1d) and given the composition of the glass (enriched in Si) it must have experienced longer cooling times. When compared to experimental data with similar Si concentration, cooling rates below 180 °C/h (cooling duration > 10h) are obtained (Vetere et al., 2015).

The estimated cooling rates are subject to uncertainties because (1) the phase abundances obtained are estimated from chemically homogeneous molten material, (2) the cooling rates are strongly dependent of the – unknown- localization of the fragment of tektite within the complete object (core vs edges), and (3) the inclusions observed in both

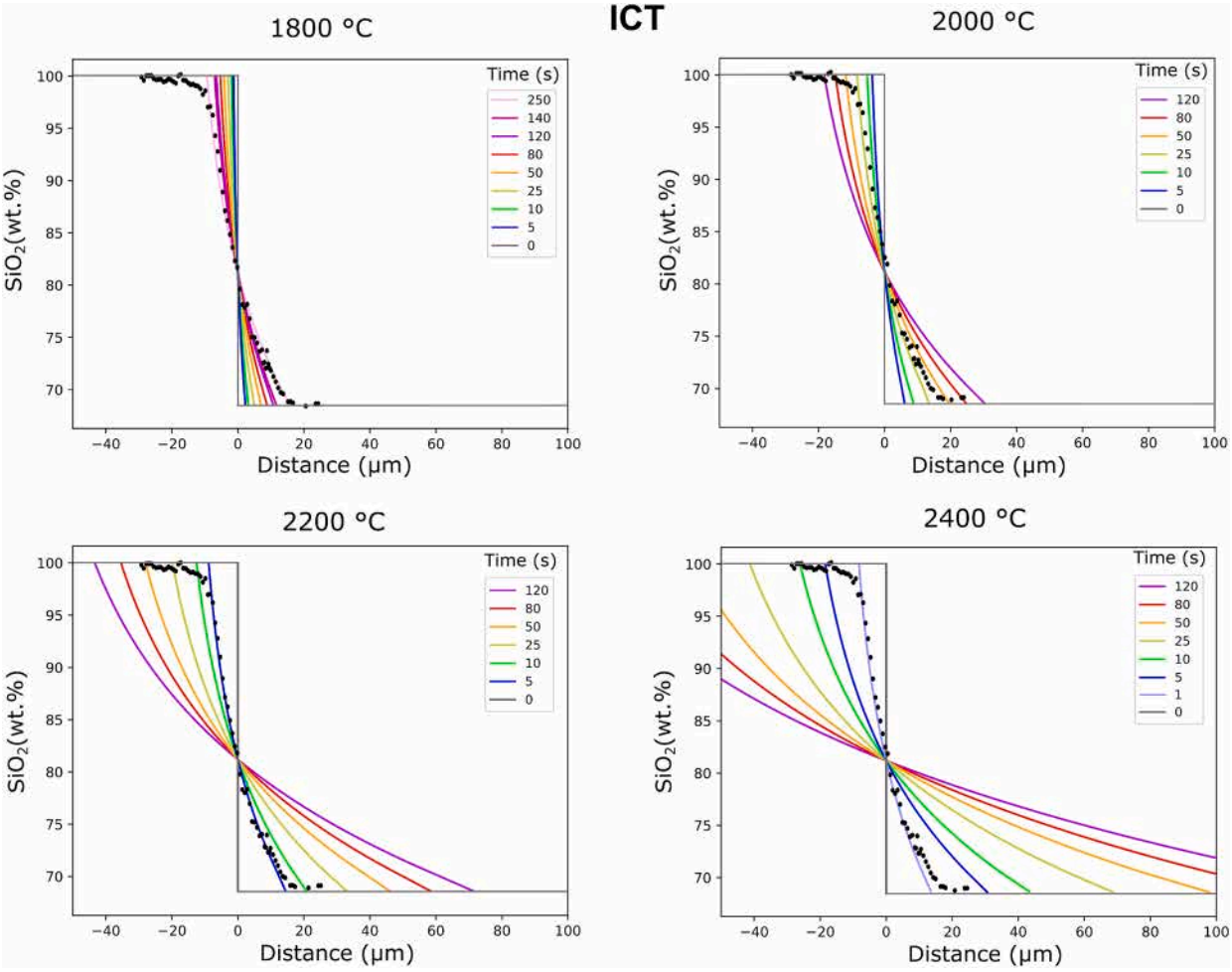

Fig. 11. Comparing data from ICT lechatelierite diffusion profile (dark circles) with a model from Macris et al., (2018). Diffusivity parameter is calculated using the equation 4 in the text to account for SiO_2 concentration variation (in each point) and this at 1800, 2000, 2200 and 2400 °C for 0–250 s (colored lines). Characteristic times of diffusion are also consistent with more simplistic model using an averaged diffusion coefficient (Fig. S13). The profiles produced using equation (2) are centered around the Matano plane (a point along the diffusion profile that defines where the areas under the concentration curve are equal on either side of a vertical plane).

tektites may be inherited from pre-existing grains that affect the local composition and favor the crystallization of neo-forming grains.

(c) Proposed scenarios for the thermal history of the two tektites

The formation of craters by high-speed impacts is the source of complex phenomena. In a brief period of time (a few seconds), the targeted rock undergoes a series of complex processes, including pre-impact heating by radiation from the plasma created by atmosphere compression, shock-induced melting of the material, and temperature buffering in the vapor plume. Each generated tektite has recorded a particular trajectory in this temperature pressure mesh. In other words, two tektites from the same impact, whose initial source is not far away, may have experienced markedly different time–temperature conditions. To facilitate interpretation of the data, given that the initial heating steps are relatively brief (of the order of a few seconds) and that we cannot distinguish the different heating mechanisms from the information recorded in the mineral inclusions, we group these mechanisms under a single denomination: impact plume development. Similarly, we have shown that the initial cooling rate is fast enough to produce dendritic spinels, and therefore we assume that the diffusion profiles are mainly formed during temperature buffering in the plume rather than during material cooling (Figs. 10-12).

After the impact, the two samples are buffered at high temperature in the vapor plume where the low viscosity contrast allows lechatelierite/host glass mixing (to decrease $\lambda = \mu_{SiO2}/\mu_{glass}$, e.g., (Fig. 13a). The cooling of a tektite is driven by by temperature-dependent heat losses at surface (σT^4) and radiative/conductive heat transfer within the tektite. Without the buffering effect of the plume, once the tektite radiates into the void or an ambient atmosphere, it can potentially reach relatively high cooling rates, depending on its size and the heat transfer inside the tektite. Diffusion profiles from lechatelierite domains demonstrate that **MN-AAT** was heated to a higher temperature or for a longer time than ICT (Fig. 11 vs Fig. 12). The MN-AAT impact crater (and therefore the energy) for the Australasian tektites is supposedly larger (>30km) than for Bosumtwi crater (10 km), suggesting that MN-AAT may have been buffered in a larger impact plume and thus for longer times. We may thus assume that the MN-AAT was heated to a temperature >2200 °C and heated for a longer time (20 s) in the vapor plume (Fig. 13b) than ICT. After this period of SiO_2 diffusion, an increase in cooling rate, for instance due to separation from the plume, stopped the homogenization of the glass. Such high cooling rates are recorded by the dendritic spinel and the magnetite-corundum intergrowth in MN-AAT (Figs. 8 and 9). Although diffusion may have occurred during this fast-cooling period, it was negligible in comparison to that during the heating period (equations 11–12). Stöffler et al., (2002) presented a numerical model for the production of moldavites associated with the Ries impact. In their model, all particles land on the surface 5–30 min after the initial impact.

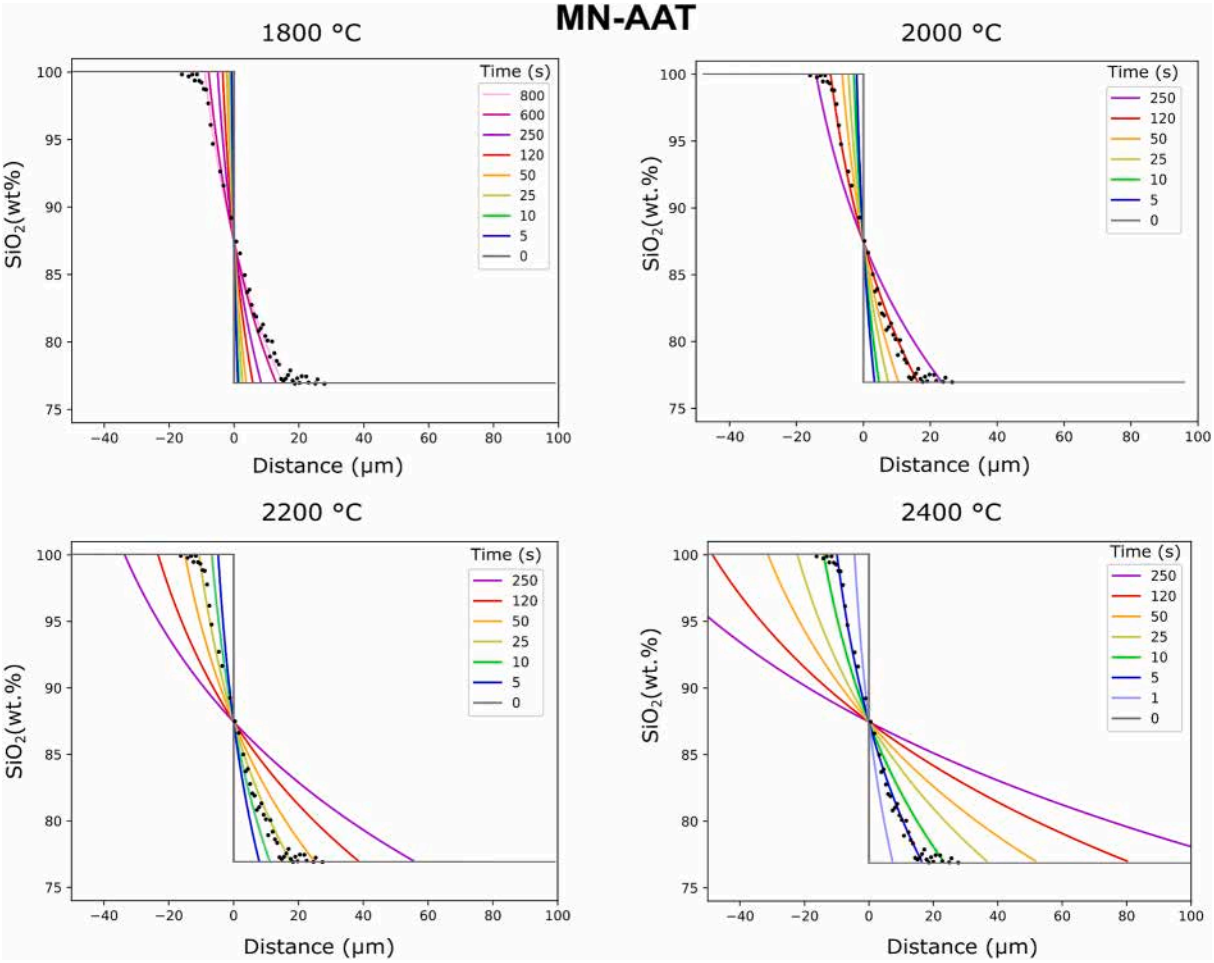

Fig. 12. Comparing data from MN-AAT lechatelierite diffusion profile (dark circles) with a model from Macris et al., (2018). Diffusivity parameter is calculated to account for SiO_2 concentration ($SiO_2 = 77$ wt%) at 1800, 2000, 2200 and 2400 °C for 0–250 s (colored lines). Lechatelierite diffuse slower for higher SiO_2 concentration. Characteristic times of diffusion are also consistent with more simplistic model using an averaged diffusion coefficient (Fig. S13). The profiles produced using equation (2) are centered around the Matano plane (a point along the diffusion profile that defines where the areas under the concentration curve are equal on either side of a vertical plane).

The characteristic cooling time that we obtained for MN-AAT (~10*h*, which is consistent with the large size of Muong Nong blocks) is far superior to the time of flight, indicating the MN-AAT tektite likely finished cooling down on the ground at slower (~200 °C/h) rates (Gattacceca et al., 2022). The reason for the slower cooling rate (compared to ICT) could be the much larger mass of the Muong-Nong type Australasite bodies, as samples up to 24 kg have been reported (Koeberl, 1992, 1994; Fiske et al., 1999). Also, the landing in a heavily vegetated area with wildfires ignited by impact plume radiation or still hot tektite melt may have slowed cooling.

In comparison, we have less information about the **ICT**, since only the lechatelierite scattering profiles and the presence of merrilite inform about the thermal history. As shown above, the time required to produce diffusion profiles is shorter than for MN-AAT (for the same nominal distance of ~20μm) because the host glass is poorer in SiO_2. Therefore, we suggest that ICT was heated above 2200 °C for a short heating time of ~5s. ICT was then exposed to fast cooling rates (inclusions are mostly made of amorphous phosphates) yet slow enough (~2000 °C/h) to start crystallizing merrillite acicular crystals.

Quantification of heating and residence times in the plume are based here on information recorded in the inclusions of both samples. However, these estimates are subject to uncertainties due to the heterogeneous nature of samples. They would be greatly improved by modelling studies of the two plumes, which would allow to estimate the ejection velocities and the propagation velocity of the impact plume.

4.2. *Origin of the phosphate minerals in Ivory Coast and MN Tektites*

(a) Inclusions inherited from pre-existing grains

Most of the mineral inclusions in tektites have been described in Australasian tektites and microtektites (Glass and Barlow, 1979; Dressler and Reimold, 2001; Folco et al., 2010; Cavosie, 2018; Cavosie et al., 2018; Křížová et al., 2019; Rochette et al., 2021; Pan et al., 2023). Those mineral inclusions are mainly quartz (lechatelierite, SiO_2), Fe-Ti oxides, silicates and refractory minerals as zircon or reidite ($ZrSiO_4$), baddeleyite (ZrO_2), rutile (TiO_2), corundum (Al_2O_3), chromite ($FeCr_2O_4$) and one phosphate mineral, monazite (Ce,La,Nd,Th)PO_4. In addition to these inclusions, "metallic spherules" mostly constituted of kamacite (FeNi), troilite (FeS) and schreibersite ($(FeNi)_3P$) were reported from several splash-form AAT (Chao et al., 1962, 1964). Recently, shenzhuangite ($NiFeS_2$) inclusions were described MN-AAT tektites by Křížová et al., (2019). Besides MN-AAT, Fe-Ti oxides inclusions have also been described in belizite (Rochette et al., 2021) while zircon and baddeleyite (ZrO_2) have been described in moldavite and North American tektites (Glass and Barlow, 1979; Glass et al., 1995). No inclusions have been described in ivorites so far, apart from lechatelierite. Phosphate inclusions have been described in Lybian desert glass (Kovaleva et al., 2023).The inclusions found in our study in the Ivory coast and Australasian tektites are the first to contain phosphate minerals (apatite and merrillite) other than the monazite crystal previously identified by Glass

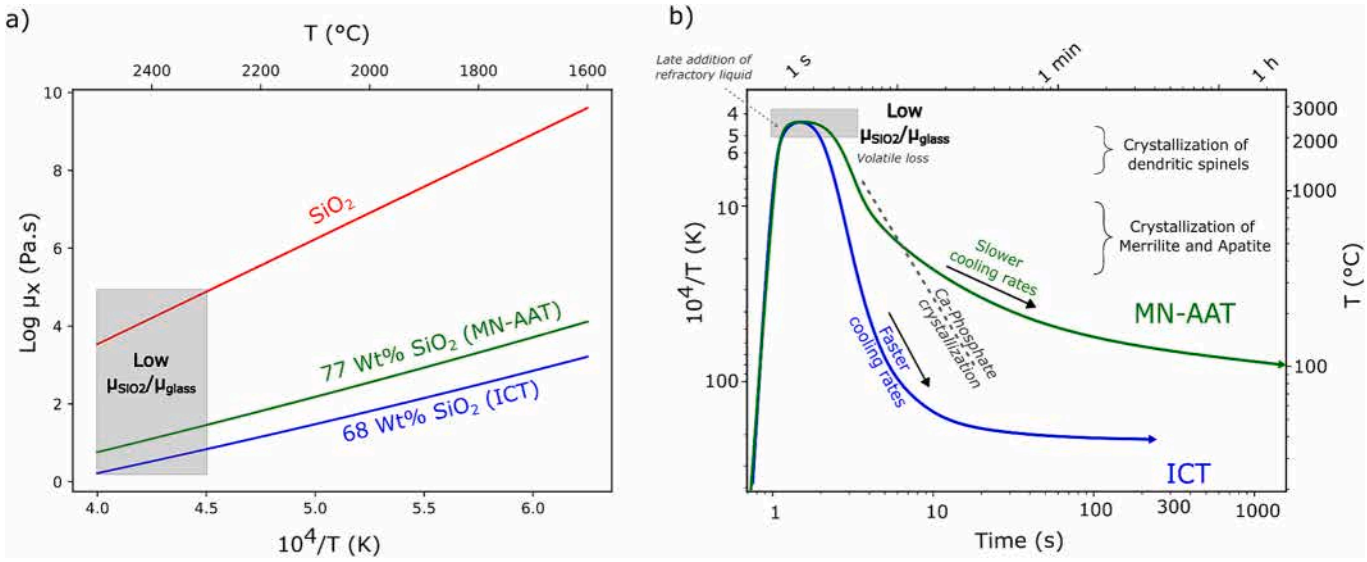

Fig. 13. a) Arrhenius plots for the viscosities of glass with various compositions. Viscosities are modeled using the three-parameter Tammann-Vogel-Fulcher (TVF) equation from (Richet 1984; Toplis et al., 1997). The gray rectangle encloses the area where viscosity ratio; $\lambda = \mu_{SiO_2}/\mu_{glass}$ is low. b) Schematic representation of the two thermal histories from ICT (blue) and MN-AAT (green) samples. Both samples are rapidly heated by the impact. MN-AAT reached a higher maximum temperature but for a short time before being ejected from the vapor plume and slowly cooled at the Earth's surface. ICT was heated to a lower temperature but remained in the plume longer, before being rapidly cooled in the atmosphere. Fe-rich glass in MN-AAT originate from a late addition of material in the glass.

and Barlow (1979) and characterized by Seydoux-Guillaume et al. (2024). The presence of such inclusions is crucial because they allow discussing the source of the material that was excavated.

The mineral inclusions in MN-AAT and ICT may be interpreted as either terrestrial in origin or as extraterrestrial material derived from a projectile that has been incorporated into the tektite glass. Nevertheless, the available evidence suggests that these inclusions are of terrestrial origin for both samples. In **MN-AAT**, the low bulk content of Ni, Co, and Cr indicates that contamination from extraterrestrial sources is unlikely. In the case of **ICT**, all the phosphate grains are contained in lechatelierite, which has long been recognized as being inherited from terrestrial material (mostly quartz grain).

Phosphates are insoluble in Si-rich melts and tend to precipitate in glass (Tollari et al., 2006). The mineral inclusions observed in this study could result from the local precipitation of the phosphorus contained in the surrounding silicate melt. In MN-AAT the precipitation could have been facilitated by the presence of a tiny (~50 nm in size) Pt-rich nucleus (Fig. 3e and S7-8). However, the bulk P_2O_5 content of the two tektites is too low to support such a scenario. It rather suggests that the inclusions in the two tektites are inherited from pre-existing grains that melted and re-crystallized. **In MN-AAT**, the exogenous origin of the inclusions is evident in Fig. 3b, where they are embedded in lechatelierites. However, they are also particularly evident in Fig. 1d, where they are systematically included in Fe-rich flow bands. One such schlieren or flow band (Fig. 3c) is an emulsion of melted pre-existing grains, mainly phosphate. The preservation of such small, partially coalesced droplets suggests immiscible liquids. The glass host in this emulsion is Fe-rich reflecting other phases in the precursor sediment. The preservation of small, partially coalesced droplets (e.g., the nanosphere observed at the SEM and TEM scale in Fig. 3a and Fig. 6) indicates the pre-existing grain was not entirely digested. The number of pre-existing grains appears to be significant and suggest that the Fe-rich liquid sampled a relatively phosphate-rich material. In ICT phosphate inclusions are systematically included in lechatelierite (Fig. 2). The systematic association of Ca-phosphate with lechatelierite grains in ICT suggests that those inclusions are derived from pre-existing grains partially digested by the glass, which have melted and recrystallized locally (Chao et al., 1962).

(b) Origins of the phosphate inclusions

Phosphate minerals are not ubiquitously distributed on the Earth's surface. The phosphorous cycle involves both biological and geological processes and phosphates occur in both worlds. Sedimentary Ca-phosphates are mainly marine sediments formed by an upwelling of phosphate-rich water into relatively shallow marine settings (Kohn et al., 2003). Such phosphate-rich water is usually produced due to high biological activity (bacteria, plankton, algae, fish). Ca-phosphates are also common minerals in many plutonic rocks, ranging from granites to the late stage cumulates of mafic systems (e.g., Bea et al., 1992; McCubbin et al., 2014; Jones et al., 2016).

The ICT case is interesting in the quest of identifying the origin of the phosphate detrital grains because the source crater has long been identified and verified (Lacroix, 1935; Koeberl et al., 1997, 1998; Soro et al., 2023). The Bosumtwi crater in Ghana, West Africa, the source crater of ivorites is excavated in 2.1–2.2 Ga old metasediments and metavolcanics of the Birrimian Supergroup. In details, the crater excavated mostly lower greenschist facies metasediments, and the metavolcanics rocks are rather situated in the southeast part of the lake. Such parent geology obviously excludes a marine sediment origin for the phosphate inclusion in the ICT. Koeberl et al., (1998) provided a comprehensive study of the excavated material. Their geochemical study of the target rocks shows that the most enriched facies is a shale with a maximum of $P_2O_5 = 0.13$ wt%. Such phosphorus content again excludes a precipitation of the phosphate rich inclusions observed in ICT from the bulk phosphorus content of the melted target material. Besides the bulk composition, Koeberl et al., (1998) also described the petrography of the rock excavated by the impact allowing to identify potential detrital grains and their abundances. They provided no description of phosphates as common or accessory mineral in the various facies. Accessory apatite has only been described in a mafic dike located NE of the Bosumtwi lake (Losiak et al., 2013). Additionally, the fact that merrillite systematically occurs only in lechatelierite in ICT is an important indicator of its potential origin. It has been widely accepted that lechatelierite were inherited from the digestion of quartz grains, thus indicating a quartz rich precursor rock (Chao et al., 1962). Yet, it is unlikely to find inclusion of phosphates within a quartz grain, especially in this abundance (Fig. 2a,b). Hydrothermal quartz–apatite veins would

be the only potential geological context where these two phases could be associated. Still, those veins are not described in the petrologic description of the target rocks by Koeberl et al., (1997) and occur almost exclusively in the southern Central Iberian Zone (e.g., Vindel et al., 2014).

An alternative hypothesis for the origin of the lechatelierite in tektites has been proposed by Kinnunen (1990). According to their model, a possible precursor of the lechatelierite is silica of plant origin in the form of biogenic opal-CT (mostly amorphous but historically considered to be composed of disordered cristobalite and tridymite) that were included in the shock-melted soil and bedrock during the impact, and formed an immiscible liquid with the host glass. Inorganic phosphate is one of the most important components of plant nutrients and can be enriched in young soil (Delgado and Torrent, 1997; Almeida et al., 2021). The association of merrillite and lechatelierite in the ICT suggest that the parent material for those inclusions is not the conventional detrital quartz grains but rather an organic silica and phosphate mixture derived from plants and residing in the soil subjected to impact melting. The surface material (association of soil and living plants) would thus explain the association of lechatelierite and phosphate inclusions in ICT (in addition to potential detrital quartz grains from excavated bedrock). A soil sample enriched in P_2O_5 with a content of 2.2 wt% was reported in the vicinity of the crater (Boamah and Koeberl, 2002). In addition, both ICT and MN-AAT are anomalously enriched in the alkali elements Ca, Na, Sr and Ba. Soil is normally depleted in alkali-earth elements, but biomass can be enriched in them (Mizera and Řanda, 2022). Geochemical measurements are thus compatible with our argument of a biomass-contaminated sedimentary target. In their paper, Mizera and Řanda (2022) advocate for a biogenic contamination in moldavites, suggesting that a future search for phosphate inclusions in these tektites could also be fruitful. A potential argument against biogenic contamination is the Na content. Mizera and Řanda (2022) showed that Na is abnormally depleted in moldavites. They interpreted this depletion as due to the differentiation of K/Na in soil profiles and suggested that it is a strong tracer of the biogenic contribution. K/Na ratio is low in ICT and relatively low in MN-AAT, or at least not that high as in moldavites. However, for ICT, the superficial material (regolith) is depleted in K, which explains the low K/Na ratio. Also, regardless of the effect of regolith composition, Na depletion also depends on the mixing proportion and composition of the sediment and biomass. As discussed in Mizera and Řanda (2022) complex fractionation processes combining vaporization and condensation in various stages of the impact and tektite formation cannot be excluded and can modify the K/Na ratio. It is beyond the scope of this paper to model those fractionation processes, but it advocates that the presence of Na does not rule out the scenario of a biogenic contribution in the case of ICT and MN-AAT. Ultimately, we suggest that the phosphate inclusions and the emulsion textures found in the Fe-rich glass (Fig. 3a-c) also formed from a similar integration of surface material in MN-AAT that later formed an association of immiscible melts.

4.3. Tektite reduction process during impact recorded by dentritic spinels

Tektites are known to be relatively reduced glasses, as shown by their low ferric to ferrous iron ratios and low (<10 ppm) ferromagnetic impurities content (e.g. Rochette et al., 2015). Iron reduction seems to be linked to the impact process (Rochette et al., 2021), but detailed clues on the process are lacking. The dendritic spinels observed in MN-AAT show a variation in composition with an Fe-rich core that crystallized starting from the Pt-rich nuclei (close to the outer boundary of the inclusion) to an Al-rich termination. Such chemical variation is accompanied with an evolution of the Fe oxidation state. The introduction of Al^{3+} in the crystalline structure as the dendrite is forming replace the Fe^{3+} and lowers the $Fe^{3+}/\sum Fe$ ratio through time. The dendritic nature of the spinel implies relatively rapid crystallization. The Pt-rich nuclei must have promoted the crystallization of spinel and the fast accommodation of the local Fe^{3+} in a few seconds (Figs. 3 e, f and 9). Similarly, the presence of corundum – magnetite (Fig. 8) intergrowth has rarely been reported in the literature but is also ascribed to important changes in redox conditions and chemical potential during fast crystallization at high temperature (Coenraads et al., 1995; Lin Sutherland et al., 1998). The decrease in oxygen fugacity must therefore have been drastic, in a matter of seconds and the dendritic spinels and magnetite-corundum intergrowths are a direct record of the reducing process that generated tektites.

Three scenarios can be proposed to explain such rapid change in fO_2. The fO_2 could have drastically decreased within the plume during the tektite's atmospheric ejection and the mineral inclusions crystalized during the ascent recording the redox variation. However, the inclusions trapped in the glass should have equilibrated with the external O_2 partial pressure in a fraction of a second. It is unlikely that the system homogenizes fast enough to change the composition of the spinels and magnetite. Another scenario that was proposed in the literature is the isentropic cooling. In this scenario, after the initial decompression, the material is a single-phase supercritical fluid. Once the pressure drops below the critical point, liquid and vapor phases appear, expand rapidly and cool isentropically. In such a system, species like Fe_2O_3 can be thermodynamically unstable and separate into oxygen gas in the vapor phase and reduced FeO or iron metal in the liquid phase. In such a scenario the whole material forming tektite is vaporized. However, total vaporization may remove the close correlations between tektites and their source rocks and destroy mineral inclusions (Koeberl, 1994). Another scenario would be that the redox reaction occurred at the time of the impact within the generated plume where chemical species could have interacted. A reaction involving a chemical species able to react with oxygen could have reduced the iron in the ejected material. Published data indicate that besides carbon gas (CO_2 and CO) trapped in tektite bubbles, another carbon reservoir is present directly in the tektite glass (Žák et al., 2012). One hypothesis for the origin of this carbon enrichment is that it was brought about by a meteoritic impact. Nevertheless, a considerable body of research has demonstrated that extraterrestrial meteoritic material in tektites is scarce (Ganapathy and Larimer, 1983; Žák et al., 2012; Ackerman et al., 2019). Another potential carbon reservoir is the terrestrial organic matter contained in the soil and plants, as previously suggested by the presence of phosphate grains in lechatelierite. Forests can bear important mass of carbon sufficient to reduce iron through a simplified reaction:

$$Fe_2O_3 + ½\ C \rightleftarrows 2\ FeO + ½\ CO_2 \quad (3)$$

Considering the typical carbon content in forest biomass of 25 kg/m^2 (Keith et al., 2009), one can compute the maximum thickness over which the reaction presented in equation (3) can affect all the Fe^{3+} present in the first meters of the Earth subsurface. Assuming a 5 wt% Fe_2O_3 content, a 7-meter-thick layer of subsurface material with density of 2 g/cm^3 may be reduced, and an even higher value may be expected if adding soil carbon. It thus appears that there is enough organic carbon to reduce the first few meters that are assumed to produce the tektites based on ^{10}Be data (Serefiddin et al., 2007; Rochette et al., 2018). Reduction of iron by soil and biomass carbon would explain the fast-reducing process recorded by the spinels at the time of the impact and a terrestrial origin of the rare metal spherules found in tektites (Ganapathy and Larimer, 1983). The presence of this surface material in addition to the excavated material could be an important component in the process of generating tektites and their geochemistry. Nevertheless, it is clear that a significant proportion of the material originates from deeper rocks and evidence of organic matter in tektites has to be documented beyond one isolated observation in a reduced impact glass (Howard et al., 2013). The $\delta^{29}Si$ and $\delta^{30}Si$ ratios of lechatelierite, in conjunction with the $^{13}C/^{12}C$ carbon ratio (in the event that traces of solid carbon matter are identified), would permit the examination of the biogenic provenance of these compounds.

5. Conclusion

The study of mineral inclusions in tektite samples from two distinct strewn fields; Ivory Coast tektites (ICT sample) and Muong Nong type Australasian tektites (MN-AAT sample) revealed the presence of Ca-phosphate inclusions. In MN-AAT, phosphates are sometimes associated with magnetite, pyroxene and spinel grown from a Pt-rich nucleus. In ICT the phosphates are systematically included in lechatelierite. Those mineral inclusions are rare in tektites and shed new lights on the thermal history and on the source material of those impact generated molten glasses. Based on our mineral characterization we concluded that MN-AAT represents an ejecta that was heated up to high temperature (2200 °C) and that was then buffered in temperature in the impact generated vapor plume for a long-enough time (20s) to produce the diffusion profile found around lechatelierite. The material then cooled down at a slower rate, after landing on the Earth surface, allowing the crystallization of large mineral inclusions (up to 10–30 μm). The ICT potentially underwent shorter buffering in the vapor plume (5s) to produce similar characteristic profile diffusion length (due to lower SiO_2 content in the host glass) and faster cooling rates (most of the inclusion's material is amorphous). However, this sample still outstands from its field with important intra-sample chemical variation evidenced by numerous schlieren and a few mineral inclusions. The nature of the inclusions found in the two tektites suggest that they may have sampled surface material enriched in P through biogenic processes. Surface material, including biomass is often ignored when discussing the origin of tektites although there is no doubt that it is an important component sampled involved by the impact during the impact process.

Data availability

Data are available through Mendeley Data at https://doi.org/10.17632/vhzjjyx2pj.1.

EDS and EELS spectrum images were processed using personal Python scripts based on Hyperspy library (**de la Peña et al. 2022**) available at: https://github.com/ZanettaPM/Ti-Oxidation-EELS-data-processing and https://github.com/ZanettaPM/TEM-Phase-map-exemple—Paris-meteorite).

CRediT authorship contribution statement

Pierre-Marie Zanetta: Writing – review & editing, Writing – original draft, Visualization, Software, Methodology, Investigation, Formal analysis, Data curation, Conceptualization. **Anne-Magali Seydoux-Guillaume:** Writing – review & editing, Validation, Supervision, Investigation, Funding acquisition, Formal analysis, Data curation, Conceptualization. **Pierre Rochette:** Writing – review & editing, Validation, Supervision, Project administration, Methodology, Investigation, Funding acquisition, Formal analysis, Data curation, Conceptualization. **Bruno Reynard:** Writing – review & editing, Validation, Supervision, Methodology, Formal analysis, Data curation. **Victor Tricaud:** Investigation, Formal analysis, Data curation. **Petanki Soro:** Investigation, Data curation. **Southone Singsoupho:** Formal analysis, Data curation. **Alain Nicaise Kouamelan:** Formal analysis, Data curation. **Obrou Monda:** Formal analysis, Data curation. **David Baratoux:** Writing – review & editing, Validation, Supervision, Methodology, Formal analysis.

Declaration of competing interest

The authors declare that they have no known competing financial interests or personal relationships that could have appeared to influence the work reported in this paper.

Acknowledgments

This work was supported by ANR ET-Megafire project (ANR-21-CE49-0014-03). The Raman facility in Lyon (France) is supported by the Institut national des sciences de l'Univers (INSU). It is a contribution of the LABEX Lyon Institute of Origins (ANR-10-LABX-0066), within the program "Investissements d'Avenir" (ANR-11-IDEX-0007) at Université de Lyon. PMZ and AMSG thank the consortium Lyon/Saint Etienne de Microscopies (CLYM) for the access to the TEM. We thank members of the LGL-TPE at Université Jean Monnet for helpful discussions. P-M. Z. thanks Yaya Lefkir, Yannick Bleu, Matthieu Lenci, Sergio Sao Joao, and Stéphanie Reynaud for their help with FEG-SEM, SEM-FIB and TEM instruments. P-M. Z. Thanks PR. Roger Hewins for useful discussions on emulsion textures and immiscible liquids. Comments of the reviewers Dr. J. Mizera, Dr. C. A. Macris and L. McGee, and of the associate editor Pr. Rhian Jones, significantly improved the manuscript and are highly appreciated.

Appendix A. Supplementary material

Additional optical, SEM and S/TEM images and EDS maps are provided in supplementary material. Supplementary material to this article can be found online at https://doi.org/10.1016/j.gca.2024.09.021.

References

Ackerman, L., Skála, R., Křížová, Š., Žák, K., Magna, T., 2019. The quest for an extraterrestrial component in Muong Nong-type and splash-form Australasian tektites from Laos using highly siderophile elements and Re-Os isotope systematics. Geochim. Cosmochim. Acta 252, 179–189.

Almeida, I.C.C., Schaefer, C.E.G.R., Fernandes, R.B.A., Oliveira, F.S., Pereira, T.T.C., 2021. Clay mineralogy and micropedology of phosphate-rich soils from Lions Rump, Maritime Antarctica. J. South Am. Earth Sci. 105, 102967.

Amare, K., Koeberl, C., 2006. Variation of chemical composition in Australasian tektites from different localities in Vietnam. Meteorit. Planet. Sci. 41, 107–123.

Barnes, V.E., 1958. Properties of tektites pertinent to their origin. Geochim. Cosmochim. Acta 14, 267–278.

Barnes, V.E., 1961. Tektites. Sci. Am. 205, 58–65.

Barnes, V.E., 1963. Detrital mineral grains in tektites. Science 142, 1651–1652.

Bea, F., Fershtater, G., Corretgé, L.G., 1992. The geochemistry of phosphorus in granite rocks and the effect of aluminium. Lithos 29, 43–56.

Boamah, D., Koeberl, C., 2002. Geochemistry of Soils from the Bosumtwi Impact Structure, Ghana, and Relationship to Radiometric Airborne Geophysical Data, 211–255.

Bulina, N.V., Avakyan, L.A., Makarova, S.V., Orehov, I.B., Bystrov, V.S., 2023. Structural features of oxyapatite. Minerals 13 (1), 102.

Cavosie, A.J., 2018. The enduring mystery of Australasian Tektites. Elements 14, 212–213.

Cavosie, A.J., Timms, N.E., Erickson, T.M., Koeberl, C., 2018. New clues from Earth's most elusive impact crater: evidence of reidite in Australasian tektites from Thailand. Geology 46, 203–206.

Chao, E.C.T., Adler, I., Dwornik, E.J., Littler, J., 1962. Metallic Spherules in Tektites from Isabela, Philippine Islands. Science 135, 97–98.

Chao, E.C.T., Dwornik, E.J., Littler, J., 1964. New data on the nickel-iron spherules from Southeast Asian tektites and their implications. Geochim. Cosmochim. Acta 28, 971–980.

Cliff, G., Lorimer, G.W., 1975. The quantitative analysis of thin specimens. J. Microsc. 103, 203–207.

Coenraads, R.R., Vichit, P., Sutherland, F.L., 1995. An unusual sapphire–zircon–magnetite xenolith from the Chanthaburi Gem Province, Thailand. Mineral. Mag. 59, 465–479.

Collins, G.S., Wünnemann, K., 2005. How big was the Chesapeake Bay impact? Insight from numerical modeling. Geology 33, 925–928.

Creech, J.B., Moynier, F., Koeberl, C., 2019. Volatile loss under a diffusion-limited regime in tektites: Evidence from tin stable isotopes. Chem. Geol. 528, 119279.

Cuttitta, F., Carron, M.K., Annell, C.S., 1972. New data on selected Ivory Coast tektites. Geochim. Cosmochim. Acta 36, 1297–1309.

de Faria, D.L.A., Venâncio Silva, S., de Oliveira, M.T., 1997. Microspectroscopy of some iron oxides raman and oxyhydroxides. J. Raman Spectrosc. 28, 873–878.

de la Peña, F., Prestat, E., Fauske, V.T., Burdet, P., Lähnemann, J., Jokubauskas, P., Furnival, T., Nord, M., Ostasevicius, T., MacArthur, K.E., and others (2022) hyperspy/hyperspy: Release v1.7.3.

Delgado, A., Torrent, J., 1997. Phosphate-rich soils in the European Union: estimating total plant-available phosphorus. Eur. J. Agron. 6, 205–214.

Dressler, B.O., Reimold, W.U., 2001. Terrestrial impact melt rocks and glasses. Earth Sci. Rev. 56, 205–284.

Engelhardt, W.V., Luft, E., Arndt, J., Schock, H., Weiskirchner, W., 1987. Origin of moldavites. Geochim. Cosmochim. Acta 51, 1425–1443.

Fiske, P.S., Schnetzler, C.C., Mchone, J., Chanthavaichith, K.K., Homsombath, I., Phouthakayalat, T., Khenthavong, B., Xuan, P.T., 1999. Layered tektites of southeast Asia: Field studies in central Laos and Vietnam. Meteorit. Planet. Sci. 34, 757–761.
Folco, L., Rochette, P., Perchiazzi, N., D'Orazio, M., Laurenzi, M.A., Tiepolo, M., 2008. Microtektites from Victoria Land Transantarctic Mountains. Geology 36, 291–294.
Folco, L., Perchiazzi, N., D'Orazio, M., Frezzotti, M.L., Glass, B.P., Rochette, P., 2010. Shocked quartz and other mineral inclusions in Australasian microtektites. Geology 38, 211–214.
Folco, L., Rochette, P., D'Orazio, M., Masotta, M., 2023. The chondritic impactor origin of the Ni-rich component in Australasian tektites and microtektites. Geochim. Cosmochim. Acta 360, 231–240.
French, B.M., 1998. Traces of Catastrophe A Handbook of Shock-Metamorphic Effects in Terrestrial Meteorite Impact Structures. Lunar and Planetary Institute, Book, LPI Contribution No. 954.
Ganapathy, R., Larimer, J.W., 1983. Nickel-iron spherules in tektites: non-meteoritic in origin. Earth Planet. Sci. Lett. 65, 225–228.
Gattacceca, J., Rochette, P., Quesnel, Y., Singsoupho, S., 2022. Revisiting the paleomagnetism of Muong Nong layered tektites: Implications for their formation process. Meteorit. Planet. Sci. 57, 558–571.
Giordano, D., Dingwell, D.B., 2003. Non-Arrhenian multicomponent melt viscosity: a model. Earth Planet. Sci. Lett. 208, 337–349.
Giuli, G., 2017. Tektites and microtektites iron oxidation state and water content. Rendiconti Lincei 28, 615–621.
Glass, B.P., 1990. Tektites and microtektites: key facts and inferences. Tectonophysics 171, 393–404.
Glass, B.P., Barlow, R.A., 1979. Mineral inclusions in Muong Nong-type indochinites: implications concerning parent material and process of formation. Meteoritics 14, 55–67.
Glass, B.P., Pizzuto, J.E., 1994. Geographic variation in Australasian microtektite concentrations: implications concerning the location and size of the source crater. J. Geophys. Res. Planets 99, 19075–19081.
Glass, B.P., Koeberl, C., Blum, J.D., Senftle, F., Izett, G.A., Evans, B.J., Thorpe, A.N., Povenmire, H., Strange, R.L., 1995. A Muong Nong-type Georgia tektite. Geochim. Cosmochim. Acta 59, 4071–4082.
Horita, Z., Sano, T., Nemoto, M., 1987. Simplification of X-ray absorption correction in thin-sample quantitative microanalysis. Ultramicroscopy 21, 271–276.
Howard, K.T., 2011. Volatile enhanced dispersal of high velocity impact melts and the origin of tektites. Proc. Geol. Assoc. 122, 363–382.
Howard, K.T., Bailey, M.J., Berhanu, D., Bland, P.A., Cressey, G., Howard, L.E., Jeynes, C., Matthewman, R., Martins, Z., Sephton, M.A., and others (2013) Biomass preservation in impact melt ejecta. Nature Geoscience 2013 6:12, 6, 1018–1022.
Humayun, M., Koeberl, C., 2004. Potassium isotopic composition of Australasian tektites. Meteorit. Planet. Sci. 39, 1509–1516.
Iakoubovskii, K., Mitsuishi, K., Nakayama, Y., Furuya, K., 2008. Thickness measurements with electron energy loss spectroscopy. Microsc. Res. Tech. 71, 626–631.
Jiang, Y., Chen, H., Fegley, B., Lodders, K., Hsu, W., Jacobsen, S.B., Wang, K., 2019. Implications of K, Cu and Zn isotopes for the formation of tektites. Geochim. Cosmochim. Acta 259, 170–187.
Jones, R.H., McCubbin, F.M., Guan, Y., 2016. Phosphate minerals in the H group of ordinary chondrites, and fluid activity recorded by apatite heterogeneity in the Zag H3–6 regolith breccia. Am. Mineral. 101, 2452–2467.
Jourdan, F., Nomade, S., Wingate, M.T.D., Eroglu, E., Deino, A., 2019. Ultraprecise age and formation temperature of the Australasian tektites constrained by 40Ar/39Ar analyses. Meteorit. Planet. Sci. 54, 2573–2591.
Keith, H., Mackey, B.G., Lindenmayer, D.B., 2009. Re-evaluation of forest biomass carbon stocks and lessons from the world's most carbon-dense forests. Proc. Nati. Acad. Sci. USA, 106, 11635–11640.
Kinnunen, K.A., 1990. Lechatelierite inclusions in indochinites and the origin of tektites. Meteoritics 25, 181–184.
Koeberl, C., 1990. The geochemistry of tektites: an overview. Tectonophysics 171, 405–422.
Koeberl, C., 1992. Geochemistry and origin of Muong Nong-type tektites. Geochim. Cosmochim. Acta 56, 1033–1064.
Koeberl, C., Bottomley, R., Glass, B.P., Storzer, D., 1997. Geochemistry and age of Ivory Coast tektites and microtektites. Geochim. Cosmochim. Acta 61, 1745–1772.
Koeberl, C., Reimold, W., Blum, JoelD, Chamberlain, C.P., 1998. Petrology and geochemistry of target rocks from the Bosumtwi impact structure, Ghana, and comparison with Ivory Coast tektites. Geochim. Cosmochim. Acta 62, 2179–2196.
Koeberl, C., Brandstätter, F., Glass, B.P., Hecht, L., Mader, D., Reimold, W.U., 2007. Uppermost impact fallback layer in the Bosumtwi crater (Ghana): Mineralogy, geochemistry, and comparison with Ivory Coast tektites. Meteorit. Planet. Sci. 42, 709–729.
Koeberl, C., Glass, B.P., Schulz, T., Wegner, W., Giuli, G., Cicconi, M.R., Trapananti, A., Stabile, P., Cestelli-Guidi, M., Park, J., 2022. Tektite glasses from Belize, Central America: Petrography, geochemistry, and search for a possible meteoritic component. Geochim. Cosmochim. Acta 325, 232–257.
Koeberl, C., 1994. Tektite origin by hypervelocity asteroidal or cometary impact. Target rocks, source craters, and mechanisms. In B.O., Dressler, R.A.F., Grieve, and V.L. Sharpton, Eds., Large Meteorite Impacts and Planetary Evolution. Vol. Special Paper 293, pp. 133–152. Geological Society of America.
Kohn, M.J., Rakovan, J., Hughes, J.M., 2003. Phosphates Geochemical, Geobiological and Materials Importance. Walter de Gruyter GmbH & Co KG., 48.
Kovaleva, E., Helmy, H., Belkacim, S., Schreiber, A., Wilke, F.D.H., Wirth, R., 2023. Libyan Desert Glass: New evidence for an extremely high-pressure-temperature impact event from nanostructural study. Am. Mineral. 108, 1906–1923.
Křížová, Š., Skála, R., Halodová, P., Žák, K., Ackerman, L., 2019. Near end-member shenzhuangite, NiFeS2, found in Muong Nong-type tektites from Laos. Am. Mineral. 104, 1165–1172.
Lacroix, A., 1935. Les tectites de l'Indochine et de ses abords et celles de la Cote d'Ivoire. Archives Du Muséum 12, 151–170.
Lafuente, B., Downs, R.T., Yang, H., Stone, N., 2015. 1. The power of databases: The RRUFF project. In Highlights in Mineralogical Crystallography Vol. Chapter 1, pp. 1–30. DE GRUYTER.
Le Guillou, C., Zanetta, P.M., Leroux, H., Blanchenet, A.M., Marinova, M., 2024. Light Element (C, N, O) Quantification by EDXS: Application to Meteorite Water Content and Organic Composition. Microsc. Microanal. 30 (4), 660–670.
Lin Sutherland, F., Hoskin, P.W.O., Fanning, C.M., Coenraads, R.R., 1998. Models of corundum origin from alkali basaltic terrains: a reappraisal. Contrib. Miner. Petrol. 133, 356–372.
Lofgren, G., Hargraves, R.B., 1980. Experimental studies on the dynamic crystallization of silicate melts. In Physics of magmatic processes Vol. 487, p. 551.
Losiak, A., Schulz, T., Buchwaldt, R., Koeberl, C., 2013. Petrology, major and trace element geochemistry, geochronology, and isotopic composition of granitic intrusions from the vicinity of the Bosumtwi impact crater, Ghana. Lithos 177, 297–313.
Lukanin, O.A., Kadik, A.A., 2007. Decompression mechanism of ferric iron reduction in tektite melts during their formation in the impact process. Geochem. Int. 45, 857–881.
Macris, C.A., Asimow, P.D., Badro, J., Eiler, J.M., Zhang, Y., Stolper, E.M., 2018. Seconds after impact: Insights into the thermal history of impact ejecta from diffusion between lechatelierite and host glass in tektites and experiments. Geochim. Cosmochim. Acta 241, 69–94.
Manga, M., 1996a. Dynamics of drops in cavity flows: Aggregation of high viscosity ratio drops. Phys. Fluids 8, 1732–1737.
Manga, M., 1996b. Mixing of heterogeneities in the mantle: Effect of viscosity differences. Geophys. Res. Lett. 23, 403–406.
Masotta, M., Peres, S., Folco, L., Mancini, L., Rochette, P., Glass, B.P., Campanale, F., Gueninchault, N., Radica, F., Singsoupho, S., 2020. 3D X-ray tomographic analysis reveals how coesite is preserved in Muong Nong-type tektites. Sci. Rep. 10, 20608.
McCubbin, F.M., Shearer, C.K., Burger, P.V., Hauri, E.H., Wang, J., Elardo, S.M., Papike, J.J., 2014. Volatile abundances of coexisting merrillite and apatite in the martian meteorite Shergotty: Implications for merrillite in hydrous magmas. Am. Mineral. 99, 1347–1354.
McMillan, P., Piriou, B., 1983. Raman spectroscopic studies of silicate and related glass structure: a review. Bull. Minér. 106, 57–75.
McMillan, P.F., Poe, B.T., Gillet, P.H., Reynard, B., 1994. A study of SiO2 glass and supercooled liquid to 1950 K via high-temperature Raman spectroscopy. Geochim. Cosmochim. Acta 58, 3653–3664.
Mizera, J., 2022. Quest for the Australasian impact crater: Failings of the candidate location at the Bolaven Plateau, Southern Laos. Meteorit. Planet. Sci. 57, 1973–1986.
Mizera, J., Řanda, Z., 2022. Geochemical indicators of a biogenic component in source materials of moldavites. In: In the Footsteps of Warren b. Hamilton: New Ideas in Earth Science, Vol. 553. Geological Society of America, pp. 335–346.
Mizera, J., Řanda, Z., Kameník, J., 2016. On a possible parent crater for Australasian tektites: geochemical, isotopic, geographical and other constraints. Earth Sci. Rev. 154, 123–137.
Morris, P.L., 1980. The correction of thin foil microanalysis data for X-ray absorption effects. Electron Microscopy Anal. 1979, 413–416.
Moynier, F., Koeberl, C., Beck, P., Jourdan, F., Telouk, P., 2010. Isotopic fractionation of Cu in tektites. Geochim. Cosmochim. Acta 74, 799–807.
Mukherjee, S., Sarkar, K., 2009. Effects of viscosity ratio on deformation of a viscoelastic drop in a Newtonian matrix under steady shear. J. Non-Newtonian Fluid Mech. 160, 104–112.
Noguchi, T., Matsumoto, T., Miyake, A., Igami, Y., Haruta, M., Saito, H., Hata, S., Seto, Y., Miyahara, M., Tomioka, N., 2023. A dehydrated space-weathered skin cloaking the hydrated interior of Ryugu. Nat. Astron 7, 170–181.
Okuno, M., Reynard, B., Shimada, Y., Syono, Y., Willaime, C., 1999. A Raman spectroscopic study of shock-wave densification of vitreous silica. Phys. Chem. Miner. 26, 304–311.
Pan, Q., Xiao, Z., Wu, Y., Shi, T., Yin, Z., Yan, P., Li, Y., 2023. Magnetic properties of Australasian tektites from South China. J. Geophys. Res. Solid Earth 128.
Pucéat, E., Reynard, B., Lécuyer, C., 2004. Can crystallinity be used to determine the degree of chemical alteration of biogenic apatites? Chem. Geol. 205, 83–97.
Richet, P., 1984. Viscosity and configurational entropy of silicate melts. Geochim. Cosmochim. Acta 48, 471–483.
Rochette, P., Gattacceca, J., Devouard, B., Moustard, F., Bezaeva, N.S., Cournède, C., Scaillet, B., 2015. Magnetic properties of tektites and other related impact glasses. Earth Planet. Sci. Lett. 432, 381–390.
Rochette, P., Braucher, R., Folco, L., Horng, C.S., Aumaître, G., Bourlès, D.L., Keddadouche, K., 2018. 10Be in Australasian microtektites compared to tektites: Size and geographic controls. Geology 46, 803–806.
Rochette, P., Beck, P., Bizzarro, M., Braucher, R., Cornec, J., Debaille, V., Devouard, B., Gattacceca, J., Jourdan, F., Moustard, F., 2021. Impact glasses from Belize represent tektites from the Pleistocene Pantasma impact crater in Nicaragua. Commun. Earth Environ. 2021 (2), 1–8.
Rochette, P., Bezaeva, N.S., Kosterov, A., Gattacceca, J., Masaitis, V.L., Badyukov, D.D., Giuli, G., Lepore, G.O., and Beck, P. (2019) Magnetic Properties and Redox State of Impact Glasses: A Review and New Case Studies from Siberia. Geosciences 2019, Vol. 9, Page 225, 9, 225.
Schaller, M.F., Fung, M.K., Wright, J.D., Katz, M.E., Kent, D.V., 2016. Impact ejecta at the Paleocene-Eocene boundary. Science 354, 225–229.

Schmieder, M., Kennedy, T., Jourdan, F., Buchner, E., Reimold, W.U., 2018. A high-precision 40Ar/39Ar age for the Nördlinger Ries impact crater, Germany, and implications for the accurate dating of terrestrial impact events. Geochim. Cosmochim. Acta 220, 146–157.

Serefiddin, F., Herzog, G.F., Koeberl, C., 2007. Beryllium-10 concentrations of tektites from the Ivory Coast and from Central Europe: Evidence for near-surface residence of precursor materials. Geochim. Cosmochim. Acta 71, 1574–1582.

Seydoux-Guillaume, A.M., Rochette, P., Gardés, E., Zanetta, P.M., Sao-Joao, S., de Parseval, P., Glass, B.P., 2024. Clues on the Australasian impact crater site inferred from detailed mineralogical study of a monazite inclusion in a Muong Nong tektite. Geology. Preprint online version.

Sheffer, A., 2007. Chemical reduction of silicates by meteorite impacts and lightning strikes.

Sieh, K., Herrin, J., Jicha, B., Angel, D.S., Moore, J.D.P., Banerjee, P., Wiwegwin, W., Sihavong, V., Singer, B., Chualaowanich, T., 2020. Australasian impact crater buried under the Bolaven volcanic field, Southern Laos. PNAS 117, 1346–1353.

Sieh, K., Angel, D.S., Herrin, J., Jicha, B., Singer, B., Sihavong, V., Wiwegwin, W., Wong, N., Quah, J.Y., 2023. Proximal ejecta of the Bolaven extraterrestrial impact, southern Laos. Proc. Nat. Acad. Sci. USA 120.

Słaby, E., Förster, H.-J., Wirth, R., Wudarska, A., Birski, Ł., Moszumańska, I., 2017. Validity of the apatite/merrillite relationship in evaluating the water content in the martian mantle: implications from Shergottite Northwest Africa (NWA) 2975. Geosciences 7, 99.

Son, T.H., Koeberl, C., 2005. Chemical variation within fragments of Australasian tektites. Meteorit. Planet. Sci. 40, 805–815.

Soro, P., Rochette, P., Baratoux, D., Nicaise Kouamelan, A., Andrieu-Ponel, V., Monda, O., 2023. Revisiting the Côte d'Ivoire tektite strewn field. J. Afr. Earth Sc.

Stöffler, D., Artemieva, N.A., Pierazzo, E., 2002. Modeling the Ries-Steinheim impact event and the formation of the moldavite strewn field. Meteorit. Planet. Sci. 37, 1893–1907.

Stone, H.A., 1994. Dynamics of drop deformation and breakup in viscous fluids. Annu. Rev. Fluid Mech. 26, 65–102.

Taylor, G.I., 1934. The formation of emulsions in definable fields of flow. Proc. Roy. Soc. Lond.. Series A, Containing Papers of a Mathematical and Physical Character, 146, 501–523.

Tollari, N., Toplis, M.J., Barnes, S.-J., 2006. Predicting phosphate saturation in silicate magmas: an experimental study of the effects of melt composition and temperature. Geochim. Cosmochim. Acta 70, 1518–1536.

Toplis, M.J., Dingwell, D.B., Hess, K.U., Lenci, T., 1997. Viscosity, fragility, and configurational entropy of melts along the join SiO2-NaAlSiO4. Am. Mineral. 82, 979–990.

Vetere, F., Iezzi, G., Behrens, H., Holtz, F., Ventura, G., Misiti, V., Cavallo, A., Mollo, S., Dietrich, M., 2015. Glass forming ability and crystallisation behaviour of sub-alkaline silicate melts. Earth Sci. Rev. 150, 25–44.

Vindel, E., Chicharro, E., Villaseca, C., López-García, J.Á., Sánchez, V., 2014. Hydrothermal phosphate vein-type ores from the southern Central Iberian Zone, Spain: evidence for their relationship to granites and Neoproterozoic metasedimentary rocks. Ore Geol. Rev. 62, 143–155.

White, W.B., Minser, D.G., 1984. Raman spectra and structure of natural glasses. J. Non Cryst. Solids 67, 45–59.

Whymark, A., 2021. A review of evidence for a Gulf of Tonkin location for the Australasian tektite source crater. Thai Geoscience Journal.

Wilding, M., Webb, S., Dingwell, D.B., 1996. Tektite cooling rates: Calorimetric relaxation geospeedometry applied to a natural glass. Geochim. Cosmochim. Acta 60, 1099–1103.

Žák, K., Skála, R., Řanda, Z., Mizera, J., 2012. A review of volatile compounds in tektites, and carbon content and isotopic composition of moldavite glass. Meteorit. Planet. Sci. 47, 1010–1028.

Zanetta, P.-M., Le Guillou, C., Leroux, H., Zanda, B., Hewins, R.H.H., Lewin, E., Pont, S., 2019. Modal abundance, density and chemistry of micrometer-sized assemblages by advanced electron microscopy: application to chondrites. Chem. Geol. 514, 27–41.

Zanetta, P.M., Leroux, H., Le Guillou, C., Zanda, B., Hewins, R.H., 2021. Nebular thermal processing of accretionary fine-grained rims in the Paris CM chondrite. Geochim. Cosmochim. Acta 295, 135–154.

Zanetta, P.M., Le Guillou, C., Leroux, H., Zanda, B., Hewins, R., Bellino, G., 2022. Processes and temperatures of FGR formation in chondrites. Geochim. Cosmochim. Acta 319, 94–117.

Zanetta, P.-M., Manga, V.R., Chang, Y.-J., Ramprasad, T., Weber, J., Beckett, J.R., Zega, T.J., 2023. Atomic-scale characterization of the oxidation state of Ti in meteoritic hibonite: Implications for early solar system thermodynamics. Am. Mineral.: J. Earth Planet. Mater. 108, 881–902.

Zhang, Y., 2009. Geochemical Kinetics, Book. Geochemical Kinetics. Princeton University Press.